Quadratic magneto-optic Kerr effect spectroscopy of Fe epitaxial films on MgO(001) substrates

Robin Silber,[1,2,3,*] Ondřej Stejskal,[1,4] Lukáš Beran,[4] Petr Cejpek,[4] Roman Antoš,[4] Tristan Matalla-Wagner,[3] Jannis Thien,[5] Olga Kuschel,[5] Joachim Wollschläger,[5] Martin Veis,[4] Timo Kuschel,[3] and Jaroslav Hamrle[4]

[1]*Nanotechnology Centre, VŠB-Technical University of Ostrava, 17. listopadu 15, 70833 Ostrava, Czech Republic*

[2]*IT4Innovations, VŠB-Technical University of Ostrava, 17. listopadu 15, 70833 Ostrava, Czech Republic*

[3]*Center for Spinelectronic Materials and Devices, Department of Physics, Bielefeld University, Universitätsstraße 25, 33615 Bielefeld, Germany*

[4]*Faculty of Mathematics and Physics, Charles University, Ke Karlovu 5, 12116 Prague, Czech Republic*

[5]*Department of Physics and Center of Physics and Chemistry of New Materials, Osnabrück University, 49076 Osnabrück, Germany*

(Received 1 May 2019; revised manuscript received 4 July 2019; published 6 August 2019)

The magneto-optic Kerr effect (MOKE) is a well known and handy tool to characterize ferro-, ferri-, and antiferromagnetic materials. Many of the MOKE techniques employ effects solely linear in magnetization $\boldsymbol{M}$. Nevertheless, a higher-order term being proportional to $\boldsymbol{M}^2$ and called quadratic MOKE (QMOKE) can additionally contribute to the experimental data. Here, we present detailed QMOKE spectroscopy measurements in the range of 0.8–5.5 eV based on a modified eight-directional method applied on ferromagnetic bcc Fe thin films grown on MgO substrates. From the measured QMOKE spectra, two further complex spectra of the QMOKE parameters G_s and $2G_{44}$ are yielded. The difference between those two parameters, known as ΔG, denotes the strength of the QMOKE anisotropy. Those QMOKE parameters give rise to the QMOKE tensor $\boldsymbol{G}$, fully describing the perturbation of the permittivity tensor in the second order in $\boldsymbol{M}$ for cubic crystal structures. We further present experimental measurements of ellipsometry and linear MOKE spectra, wherefrom permittivity in the zeroth and the first order in $\boldsymbol{M}$ are obtained, respectively. Finally, all those spectra are described by *ab initio* calculations.

DOI: 10.1103/PhysRevB.100.064403

I. INTRODUCTION

Ferromagnetic (FM) materials have been extensively studied due to their essential usage in data storage industry. Recently, attention has been attracted to antiferromagnetic (AFM) materials due to the new possibility to control AFM spin orientation with an electrical current (based on spin-orbit torque effects) [1,2]. Hence, there is increasing demand for fast and easily accessible methods for AFM magnetization state characterization. However, most of the methods that are used for FM research are not applicable to AFM materials due to their lack of net magnetization. Nevertheless, the magneto-optic Kerr effect (MOKE) [3] and magneto-optic (MO) effects in general, which are very powerful tools used in the field of FM research, can also be employed in AFM research [4]. Although MOKE linear-in-magnetization (LinMOKE), being polar MOKE (PMOKE), longitudinal MOKE (LMOKE), and transversal MOKE (TMOKE) are only applicable to canted AFM and AFM dynamics [5–7], it is the quadratic-in-magnetization part of the MOKE (QMOKE) that is employable for fully compensated AFM [8].

There are several MO effects quadratic in magnetization. The QMOKE denotes a MO effect originating from nonzero off-diagonal reflection coefficients (r_{sp} or r_{ps}), which appear due to the off-diagonal permittivity tensor elements (such as ε_{xy}). On the other hand, magnetic linear dichroism (MLD) and birefringence (also called the Voigt or Cotton-Mouton effect) denote MO effects observed in materials where different propagation and absorption of two linearly polarized modes occur, one being parallel and the other perpendicular to the magnetization vector $\boldsymbol{M}$ [or antiferromagnetic (Néel) vector $\boldsymbol{L}$ in the case of AFM]. These effects originate from different diagonal elements of the permittivity tensor (for example, $\varepsilon_{xx} - \varepsilon_{yy}$ for light propagating along the z direction in the isotropic sample with in-plane $\boldsymbol{M}$ when $M_x \neq M_y$).

A more comprehensive approach to QMOKE is available, which also takes into account the anisotropy of QMOKE effects. Individual contributions to QMOKE can be measured and analyzed, stemming from the quadratic MO tensor $\boldsymbol{G}$ [9], which describes a change to the permittivity tensor of the crystal in the second order in $\boldsymbol{M}$. The separation algorithm (known as the eight-directional method) has been developed for cubic (001) oriented crystals [10]. It is based on MOKE measurement under eight different $\boldsymbol{M}$ directions for different sample orientations with respect to the plane of incidence. Although applying this method on AFMs would be considerably challenging (because magnetic moments of AFMs have to be reoriented to desired directions), it is not in principle impossible. The switching of AFM through inverse MO effects is possible [6,11] and control of AFM domain distribution was demonstrated by polarization-dependent optical annealing [12]. However, the easiest way to apply above mentioned separation process on AFMs would be to use easy-plane AFMs such as NiO(111) where a sufficiently large magnetic field will align the moments perpendicular to the field direction due to Zeeman energy reduction by a small

*silber.rob@gmail.com

canting of the moments [13]. Furthermore, if we take advantage of exchange coupling to an adjacent FM layer, e.g., $Y_3Fe_5O_{12}$ (YIG) [14,15], the requirement on the magnetic field strength will be substantially lower.

Nevertheless, to employ QMOKE measurements on a regular basis, the underlying origin of QMOKE must be well understood. Although QMOKE effects have been already studied, especially in the case of Heusler compounds [16–23], all the studies employ single wavelengths only. The MOKE spectroscopy together with *ab initio* calculations is an appropriate combination to gain a good understanding of the microscopic origin of MO effects. In the field of LinMOKE spectroscopy, much work has already been done [24–35], but in the field of QMOKE spectroscopy, only few systematic studies have been done so far [36,37] where non of those studies is based on our approach to QMOKE spectroscopy.

Our separation process of different QMOKE contributions is stemming from the eight-directional method [10], but we use a combination of just four directions and a sample rotation by 45° as will be described later in the text. This approach allows us to isolate QMOKE spectra that stem mostly from individual MO parameters and thus subsequently determine spectral dependencies of $G_s = G_{11} - G_{12}$ and $2G_{44}$, denoting MO parameters quadratic in $\boldsymbol{M}$ [17,38–40]. Therefore we start our study on FM bcc Fe thin films grown on MgO(001) substrates to get a basic understanding of QMOKE spectroscopy for further studies of AFMs. In the case of FM materials, we can simply orient the direction of $\boldsymbol{M}$ by using a sufficiently large external magnetic field and then separate different QMOKE contributions. We present a careful and detailed study of the MO parameters yielding process, and discuss all the experimental details that have to be considered in the process. We also present a comparison to the *ab initio* calculations and values that have been reported in the literature so far. Possible sources of deviations between reported values are discussed.

Note that speaking of MOKE in general within this paper, we understand effects in the extended visible spectral range. There is a vast number of other magnetotransport phenomena in different spectral ranges. In the dc spectral range, we can mention the well known anomalous Hall effect [41], being linear in $\boldsymbol{M}$, and anisotropic magnetoresistance (AMR) [42] together with the planar Hall effect, both being quadratic in $\boldsymbol{M}$. Recently, in the terahertz region, an MO effect of free carriers, the so-called optical Hall effect [43], has also received much attention [44]. From the x-ray family, there is the well known x-ray magnetic circular (linear) dichroism and birefringence, being linear (quadratic) in $\boldsymbol{M}$ [45,46]. All those (and other) effects (together with LinMOKE and QMOKE) can be described by equal symmetry arguments, predicting the permittivity tensor contributions of the first and second order in $\boldsymbol{M}$ [9]. The same argumentation is valid for other transport phenomena induced, e.g., by heat. Here, thermomagnetic effects such as the anomalous Nernst effect (linear in $\boldsymbol{M}$) [47–49] and the anisotropic magnetothermopower together with the planar Nernst effect (quadratic in $\boldsymbol{M}$) [50–52] define the thermopower (or Seebeck) tensor.

In the upcoming Sec. II, a brief introduction to the theory of linear and quadratic MOKE is presented. In Sec. III, we describe the sample preparation together with structural and magnetic characterization. Section IV provides the optical characterization and Sec. V the MO characterization of the samples, being LinMOKE and QMOKE spectroscopy together with QMOKE anisotropy measurements. Finally, in Sec. VI, we compare our experimental findings with *ab initio* calculations and the literature.

II. THEORY OF LINEAR AND QUADRATIC MOKE

The complex Kerr angle $\Phi_{s/p}$ for s and p polarized incident light is defined as [53,54]

$$\Phi_s = -\frac{r_{ps}}{r_{ss}} = \frac{\tan\theta_s + i\tan\epsilon_s}{1 - i\tan\theta_s\tan\epsilon_s} \approx \theta_s + i\epsilon_s,$$
$$\Phi_p = \frac{r_{sp}}{r_{pp}} = \frac{\tan\theta_p + i\tan\epsilon_p}{1 - i\tan\theta_p\tan\epsilon_p} \approx \theta_p + i\epsilon_p. \tag{1}$$

Here, $\theta_{s/p}$ and $\epsilon_{s/p}$ are Kerr rotation and Kerr ellipticity, respectively. As $|\Phi_{s/p}| < 1°$ for transition metals [30], one can use small angle approximation in Eq. (1). The reflection coefficients $r_{ss}, r_{ps}, r_{sp}, r_{pp}$ are the elements of the reflection matrix $\boldsymbol{R}$ of the sample described by the Jones formalism [54] as

$$\boldsymbol{R} = \begin{bmatrix} r_{ss} & r_{sp} \\ r_{ps} & r_{pp} \end{bmatrix}. \tag{2}$$

These reflection coefficients fundamentally depend on the permittivity tensor $\boldsymbol{\varepsilon}$ (second rank 3×3 tensor) of the magnetized crystal [53]. Elements ε_{ij} of the permittivity tensor are complex-valued functions of photon energy, and its real and imaginary part corresponds to dispersion and absorption of the material, respectively. Changes in the permittivity tensor with $\boldsymbol{M}$ can be described through the Taylor series: $\boldsymbol{\varepsilon} = \boldsymbol{\varepsilon}^{(0)} + \boldsymbol{\varepsilon}^{(1)} + \boldsymbol{\varepsilon}^{(2)} + \ldots$, where the superscript denotes the order in $\boldsymbol{M}$. In our work, we ignore all the contributions of third and higher orders in $\boldsymbol{M}$, expressing the elements of the permittivity tensor $\boldsymbol{\varepsilon}$ as

$$\varepsilon_{ij} = \varepsilon_{ij}^{(0)} + \underbrace{K_{ijk}M_k}_{\varepsilon_{ij}^{(1)} \to \text{LinMOKE}} + \underbrace{G_{ijkl}M_kM_l}_{\varepsilon_{ij}^{(2)} \to \text{QMOKE}}, \tag{3}$$

where M_k and M_l are the components of the normalized $\boldsymbol{M}$. K_{ijk} and G_{ijkl} are the components of the so-called linear and quadratic MO tensors $\boldsymbol{K}$ and $\boldsymbol{G}$ of the third and fourth rank, respectively [9]. In Eq. (3), the Einstein summation convention is used. Thus the permittivity $\boldsymbol{\varepsilon}$ up to the second order in $\boldsymbol{M}$ is fully described. The general shape of $\boldsymbol{K}$ and $\boldsymbol{G}$ can be substantially simplified using the Onsager relation $\varepsilon_{ij}(\boldsymbol{M}) = \varepsilon_{ji}(-\boldsymbol{M})$ and symmetry arguments of the material [9]. The form of these tensors for all crystallographic classes was thoroughly studied by Štefan Višňovský [53]. A cubic crystal structure with inversion symmetry (e.g., bcc Fe as investigated in this work) simplifies the permittivity tensor by

$$\varepsilon_{ij}^{(0)} = \delta_{ij}\varepsilon_d, \tag{4a}$$
$$K_{ijk} = \epsilon_{ijk}K, \tag{4b}$$
$$G_{iiii} = G_{11}, \tag{4c}$$
$$G_{iijj} = G_{12}, \qquad i \neq j, \tag{4d}$$
$$G_{1212} = G_{1313} = G_{2323} = G_{44}, \tag{4e}$$

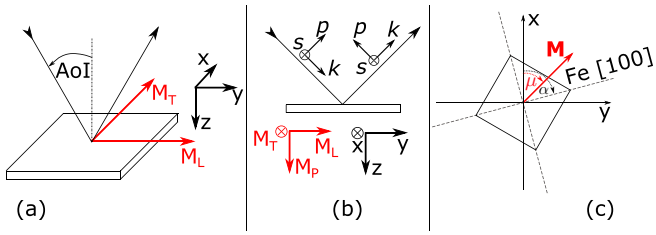

FIG. 1. (a) The right-handed coordinate system $\hat{x}$, $\hat{y}$, $\hat{z}$ is established with respect to the plane of incidence and surface of the sample. Components of the in-plane normalized magnetization M_T and M_L are defined along the axes $\hat{x}$ and $\hat{y}$ of the coordinate system, respectively. (b) Definition of the right-handed Cartesian system $\hat{s}$, $\hat{p}$, $\hat{k}$ of incident and reflected beam. (c) Definition of positive in-plane rotation of the sample and magnetization within the $\hat{x}$, $\hat{y}$, $\hat{z}$ coordinate system, described by angle α and μ, respectively.

with δ_{ij} and ϵ_{ijk} being the Kronecker delta and the Levi-Civita symbol, respectively. Hence, $\varepsilon_{ij}^{(0)}$ is a diagonal tensor described by a scalar ε_d for each photon energy. The linear MO tensor $\boldsymbol{K}$ is described by one free parameter K, whereas the quadratic MO tensor $\boldsymbol{G}$ is determined by two free parameters $G_s = (G_{11} - G_{12})$ and $2G_{44}$. In the literature, $\Delta G = G_s - 2G_{44}$ is also used [17,39], denoting the anisotropic strength of the $\boldsymbol{G}$ tensor. The shape of these tensors for cubic crystals and its dependence on the crystal orientation are intensively discussed in the literature [9,40]. The physical meaning of G_s and $2G_{44}$ is the following: G_s, $2G_{44}$ denote magnetic linear dichroism when magnetization is along the $\langle 100 \rangle$ and $\langle 110 \rangle$ directions, respectively. Namely, $G_s = \varepsilon_{\parallel} - \varepsilon_{\perp}$ for $\boldsymbol{M} \parallel \langle 100 \rangle$ and $2G_{44} = \varepsilon_{\parallel} - \varepsilon_{\perp}$ for $\boldsymbol{M} \parallel \langle 110 \rangle$, where the parallel ($\parallel$) and perpendicular ($\perp$) symbols denote the directions of linear light polarization (i.e., applied electric field) with respect to the magnetization direction, respectively [40].

Let us briefly introduce the most important sign conventions. All definitions are based on a right-handed $\hat{x}$, $\hat{y}$, $\hat{z}$ coordinate system as sketched in Fig. 1 with the $\hat{z}$ axis being normal to the sample surface (i.e., along Fe[001]) and pointing into the sample. The $\hat{y}$ axis is parallel with the plane of light incidence and with the sample surface, while its positive direction is defined by the direction of k_y, being the $\hat{y}$ component of the wave vector of incident light. The orientation of the sample is then described by an angle α, being the angle between the Fe [100] direction and the $\hat{x}$ axis of the coordinate system. Transverse, longitudinal, and polar components of the normalized magnetization M_T, M_L, and M_P are defined along the $\hat{x}$, $\hat{y}$, and $\hat{z}$ axes, respectively. Further, sign conventions are discussed in Appendix A.

The analytical approximation for FM layers relating MOKE with the permittivity of the layer is [17]

$$\Phi_s = -\frac{r_{ps}}{r_{ss}} = A_s\left(\varepsilon_{yx} - \frac{\varepsilon_{yz}\varepsilon_{zx}}{\varepsilon_d}\right) + B_s\varepsilon_{zx},$$
$$\Phi_p = \frac{r_{sp}}{r_{pp}} = -A_p\left(\varepsilon_{xy} - \frac{\varepsilon_{zy}\varepsilon_{xz}}{\varepsilon_d}\right) + B_p\varepsilon_{xz}, \qquad (5)$$

with the weighting optical factors $A_{s/p}$ and $B_{s/p}$ being even and odd functions of the angle of incidence (AoI), respectively.

In the following, we limit ourselves to in-plane normalized magnetization

$$\frac{\boldsymbol{M}}{\|\boldsymbol{M}\|} = \begin{bmatrix} M_T \\ M_L \\ 0 \end{bmatrix} = \begin{bmatrix} \cos\mu \\ \sin\mu \\ 0 \end{bmatrix}, \qquad (6)$$

where μ is the angle between the $\boldsymbol{M}$ direction and $\hat{x}$ axis of the coordinate system (see Fig. 1). From Eqs. (3)–(6), the dependence of $\Phi_{s/p}$ on K, G_s, $2G_{44}$ and on the angles α and μ can be derived as [17,39,55]

$$\Phi_{s/p} = \pm A_{s/p}\left\{\frac{2G_{44}}{4}[(1+\cos 4\alpha)\sin 2\mu - \sin 4\alpha \cos 2\mu] + \frac{G_s}{4}[(1-\cos 4\alpha)\sin 2\mu + \sin 4\alpha \cos 2\mu]\right\} \mp A_{s/p}\frac{K^2}{2\varepsilon_d}\sin 2\mu \pm B_{s/p}\,K\sin\mu. \qquad (7)$$

A change of the sign $\pm$ is related to the incident s/p polarized light beam. From this expression, measurement sequences providing MOKE spectra originating mostly from individual MO parameters are developed [10] and presented in Sec. V.

III. PREPARATION, STRUCTURAL AND MAGNETIC ANISOTROPY CHARACTERIZATION OF THE SAMPLES

A series of epitaxial bcc Fe(001) thin films with various thicknesses were prepared in an Ar atmosphere of 2.1×10^{-6} bar using magnetron sputtering. The Fe layer was directly grown on the MgO(001) substrate with a growth rate of 0.25 nm/s. To prevent oxidation, the Fe layer was capped with approximately 2.5 nm of silicon under the same conditions and with a growth rate of 0.18 nm/s. A reference sample of the MgO substrate with only silicon capping was prepared in order to determine the optical parameters of the capping layer independently. The sample set contains ten samples with a nominal thickness of the Fe layer ranging from 0 to 30 nm as shown in Table I. Furthermore,

TABLE I. Thicknesses and roughnesses of the samples, as determined from XRR. Thicknesses of Fe layer d_{Fe} and capping layer d_{cap} are very robust parameters of the fit and the value for the error bars is ±0.2 nm. Although changes of the roughness σ in tens of percent provide insignificant change to the result, it is clear that the roughness is very low as suggested in Fig. 3, and the estimated value for the error bars is ±0.5 nm.

Nominal thickness (nm)	d_{Fe} (nm)	d_{cap} (nm)	σ_{MgO} (nm)	σ_{Fe} (nm)	σ_{cap} (nm)
0.0 nm	-	3.4	0.2	-	0.3
2.5 nm	2.5	2.1	0.4	0.0	0.0
5.0 nm	4.7	2.4	0.0	0.4	0.2
7.5 nm	6.9	2.5	0.0	0.3	0.4
10.0 nm	9.4	2.7	0.2	0.0	0.6
12.5 nm	11.5	2.5	0.1	0.3	0.3
15.0 nm	14.0	2.5	0.0	0.2	0.1
20.0 nm	18.4	2.6	0.1	0.0	0.5
25.0 nm	23.3	2.4	0.1	0.2	0.6
30.0 nm	28.3	2.5	0.0	0.0	0.6

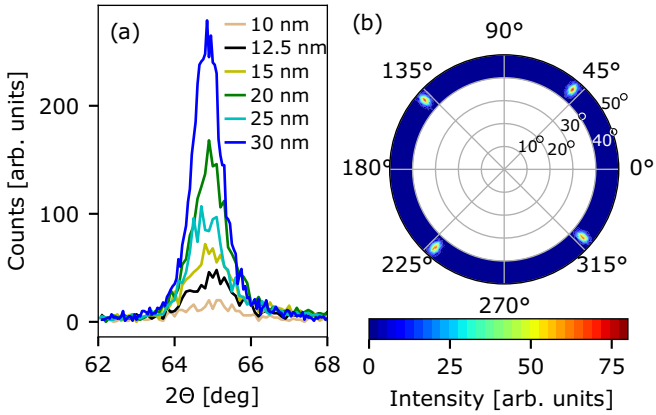

FIG. 2. (a) XRD Θ-2Θ scans of the samples with a nominal thickness > 10 nm. Thinner samples do not provide sufficient peak intensity. (b) An off-specular XRD scan (Euler's cradle texture map) is presented for the Fe{110} peaks at $2\Theta = 44.738^\circ$ of the sample with a nominal thickness of 20 nm. The measurement was performed for full 360° sample rotation (angular axis of the plot) with the tilt of the sample $\Psi = \langle 40^\circ, 50^\circ \rangle$ (radial axis of the plot).

an additional set of Fe samples grown by molecular beam epitaxy (MBE) on MgO(001) substrates and capped with Si were prepared to investigate the influence of the deposition process on the MO properties of Fe. Their preparation and comparison with the sputtered samples is discussed in Appendix C.

To verify crystallographic ordering and quality, Phillips X'pert Pro MPD PW3040-60 using a Cu K_α source was employed. X-ray diffraction (XRD) Θ-2Θ scans were performed around $2\Theta = 65^\circ$, which is the position of the characteristic Fe(002) Bragg peak. Thinner samples provide very weak peaks due to the lack of the material in the thin layers as presented in Fig. 2(a). Furthermore, for the sample with a nominal thickness of 20 nm, an off-specular texture mapping was performed using a Euler cradle [Fig. 2(b)]. During this scan the Fe{110} peak at $2\Theta = 44.738^\circ$ was used and we scanned Ψ in the range of 40°–50° with full 360° rotation of φ, where Ψ and φ are the tilt angle of the Euler cradle and the rotation angle of the sample around its surface normal, respectively. The result implies that the Fe layer within the sample is of good crystalline quality, showing a diffraction pattern in fourfold symmetry.

The thickness of each layer and the roughness of each interface was characterized by x-ray reflectivity (XRR) using the same diffractometer as for the XRD measurements. To analyze the XRR curves, the open-source program GENX [56] based on the Parratt algorithm [57] was used. XRR scans are shown for selected samples in Fig. 3. The periodicity of the oscillations is described very well by the model, providing reliable information about the thickness values of the Fe layers d_{Fe} and the capping layers d_{cap}. The densities of the layers were fixed parameters of the fit and all values were taken from the literature [58,59]. The thickness of the native silicon oxide could not be clearly determined by the XRR technique as Si and SiO_x have very similar densities. Hence,

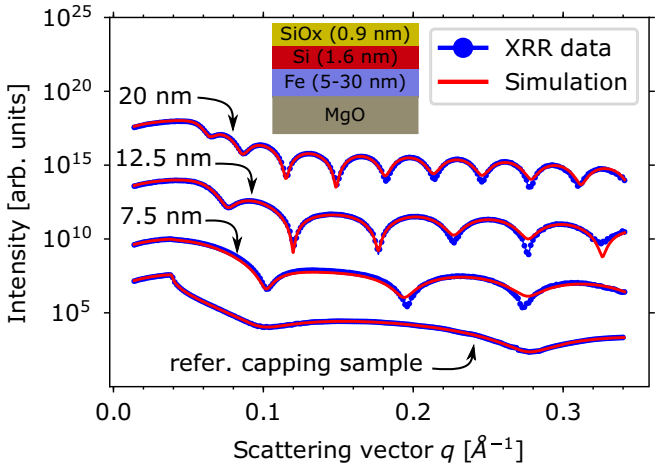

FIG. 3. Selected XRR scans (blue dots) and their simulation (red line) for several samples from the series. The periodicity of oscillations is well described, providing us with reliable information about the thickness of the layers in the samples. The damping of oscillations is low, suggesting low roughness of the interfaces within the samples. The curves are shifted vertically for clarity.

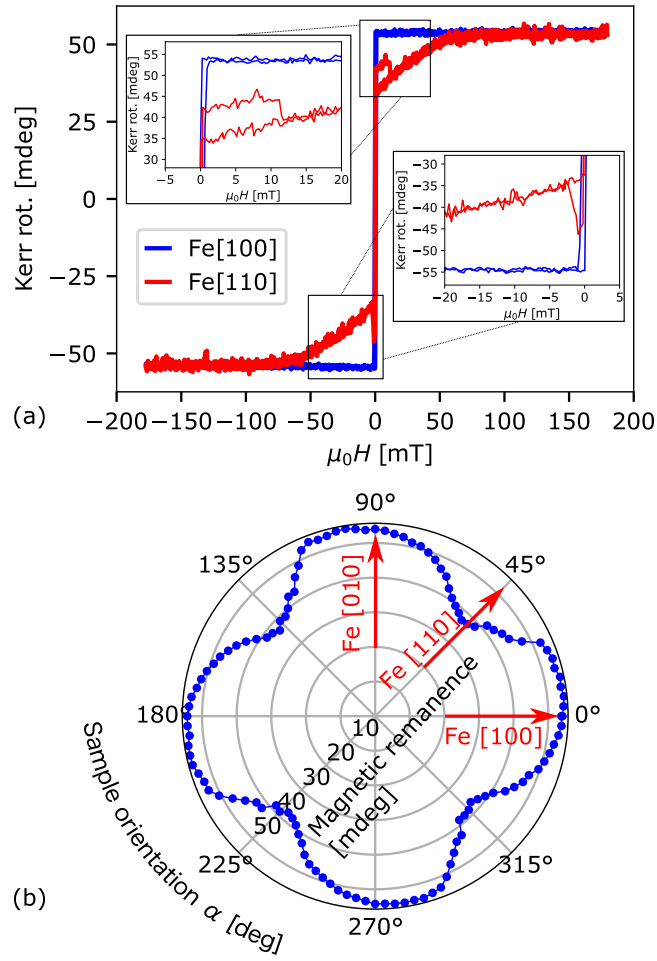

FIG. 4. Magnetic characterization of the sample with a nominal thickness of 12.5 nm. (a) The LMOKE hysteresis loops at Fe[100] and Fe[110] external field directions. About 75 mT is sufficient to saturate the sample in the in-plane hard axis. (b) In-plane magnetic remanence, with the in-plane magnetic easy and hard axes along Fe⟨100⟩ and Fe⟨110⟩ directions, respectively.

the thickness of the oxide was estimated (0.9 nm) with respect to the growth dynamics of the native silicon oxide [60]. Table I summarizes all the values of the thickness and roughness provided by the XRR data fit.

LMOKE hysteresis curves with an external magnetic field along Fe[100] and Fe[110] directions measured at $\lambda = 670$ nm (1.85 eV) are shown in Fig. 4(a). The anisotropy of the magnetic remanence (an average value of positive and negative remanence) presented in Fig. 4(b) indicates the four-fold cubic magnetocrystalline anisotropy with the magnetic easy and hard axes along the Fe⟨100⟩ and Fe⟨110⟩ directions, respectively. Figure 4(b) further suggests that magnetic easy and hard axes are rotated slightly counter-clockwise with respect to Fe⟨100⟩ and Fe⟨110⟩ directions, respectively. This could be explained by a slight misalignment of the sample in the setup with respect to $\alpha = 0°$, but more probably by additional QMOKE contributions to the LMOKE loops as identified in the inset of Fig. 4(a). The magnetic field of $\approx$75 mT is enough to saturate the sample in a magnetic in-plane hard axis, hence the in-plane magnetic field of 300 mT used within QMOKE spectroscopy is more than sufficient to keep the sample saturated with any in-plane $\boldsymbol{M}$ direction.

IV. OPTICAL CHARACTERIZATION

The Mueller matrix ellipsometer Woolam RC2 was employed to determine spectral dependencies of ε_d for all the layers within the investigated samples in the spectral range 0.7–6.4 eV. Spectra of ε_d of Fe were determined by a multilayer optical model [61], processed using COMPLETEEASE software [62]. The thicknesses and roughnesses of the constituent layers were determined by XRR measurements. The permittivity of MgO and native SiO_x was taken from the literature [63]. From the measurement of the reference sample (MgO with the Si capping only, with nominal Fe thickness 0 nm), the permittivity of the Si layer was obtained. Hence, for all the remaining samples, ε_d of the Fe layer was the only unknown and free variable of the fit.

The spectra of the imaginary part of ε_d for Fe and Si layers were described by B-spline [64], while complementary spectra of the real part were determined through Kramers-Kronig relations. The B-spline is a fast and sturdy method for determining spectra of ε_d, but does not provide direct information about the electronic structure of the material. The resulting spectra of the real and imaginary parts of Fe layers are presented in Figs. 5(a) and 5(b), respectively. The sample with a nominal thickness of 2.5 nm is deviating from the others, probably due to low crystallographic quality of the film. Although the characteristic peak at 2.5 eV in ε_d imaginary spectra of the Fe layer is not present in the spectra of Fe by Palik [63], the position of this peak is consistent with other reports as shown in Sec. VI.

V. MAGNETO-OPTIC CHARACTERIZATION

Three in-house built MOKE setups were employed to measure the LinMOKE and QMOKE response on the sample series. One setup (located at Bielefeld University) detects the MOKE with variation of the sample orientation α for a fixed photon energy 1.85 eV. Two other setups detect spectra of MOKE for a fixed sample orientation, measuring in the spectral range of 1.6–4.9 eV (Charles University in Prague) and 1.2–5.5 eV (Technical University of Ostrava), respectively, with perfect agreement of spectra obtained from both setups. The sample with a nominal thickness of 12.5 nm was later remeasured with an enhanced spectral range of 0.8–5.5 eV. A detailed description of the spectroscopic setup at the University of Ostrava can be found in the literature [65].

We now describe the QMOKE spectra measurement process. Using Eq. (7) (describing the Kerr effect dependence on the angles α, μ and the MO parameters K, G_s, and $2G_{44}$), we derive a measurement procedure separating MOKE contributions originating mostly from individual elements of the linear and quadratic MO tensors, $\boldsymbol{K}$ and $\boldsymbol{G}$, respectively. With the specified AoI and sample orientation α, we measure MOKE with several in-plane $\boldsymbol{M}$ directions [10]. To rotate $\boldsymbol{M}$ in the plane of the sample, a magnetic field of 300 mT is used and secures that the sample is always in magnetic saturation as proven in Fig. 4. Three MO contributions can be separated.

$$\text{QMOKE} \sim G_s = Q_s: \quad \Phi_{s/p}^{\mu=45°} + \Phi_{s/p}^{\mu=225°} - \Phi_{s/p}^{\mu=135°} - \Phi_{s/p}^{\mu=315°} \approx \pm 2A_{s/p}\left(G_s - \frac{K^2}{\varepsilon_d}\right), \quad \begin{matrix}\alpha = 45° \\ \text{AoI} = 5°\end{matrix}, \tag{8a}$$

$$\text{QMOKE} \sim 2G_{44} = Q_{44}: \quad \Phi_{s/p}^{\mu=45°} + \Phi_{s/p}^{\mu=225°} - \Phi_{s/p}^{\mu=135°} - \Phi_{s/p}^{\mu=315°} \approx \pm 2A_{s/p}\left(2G_{44} - \frac{K^2}{\varepsilon_d}\right), \quad \begin{matrix}\alpha = 0° \\ \text{AoI} = 5°\end{matrix}, \tag{8b}$$

$$\text{LMOKE} \sim K: \quad \Phi_{s/p}^{\mu=90°} - \Phi_{s/p}^{\mu=270°} \approx \pm 2B_{s/p}K, \quad \begin{matrix}\alpha = \text{arb. angle} \\ \text{AoI} = 45°\end{matrix}, \tag{8c}$$

where $\pm$ denotes s/p MOKE effects. The AoI in the equations were chosen with respect to the AoI dependence of the optical weighting factors $A_{s/p} \sim \cos(\text{AoI})$ and $B_{s/p} \sim \sin(\text{AoI})$. Hence, the AoI in Eqs. (8a)–(8c) only affects the amplitude of the acquired spectra and is not essential for the spectra separation process, unlike the sample orientation α and the magnetization directions μ that are vital to the measurement sequences. QMOKE and LMOKE spectra were measured at AoI = 5° and 45°, respectively.

QMOKE and LMOKE measurement sequences are determined by Eqs. (8a)–(8c), left side, as a difference of MOKE effects for different magnetization orientations μ at specified sample orientations α. We further use the denominations Q_s and Q_{44} for those QMOKE measurement sequences in Eqs. (8a) and (8b), respectively. The right side of

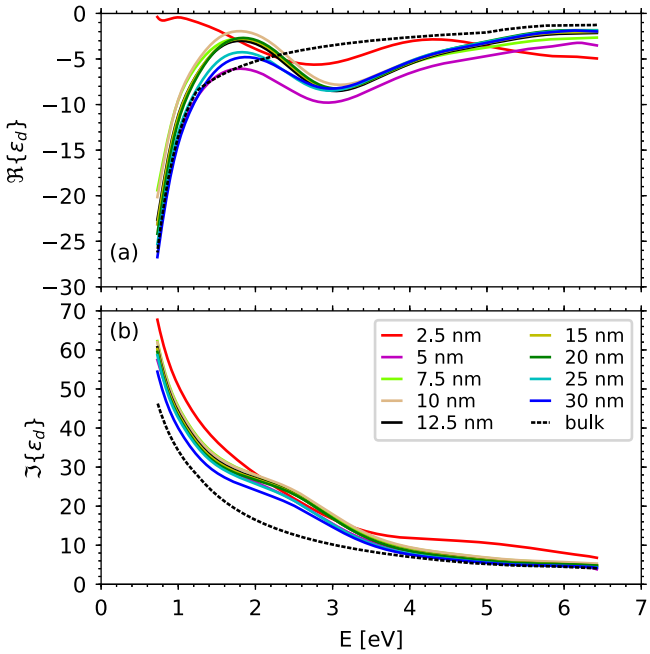

FIG. 5. The (a) real and (b) imaginary parts of ε_d of Fe layers. Black dashed lines are the ε_d of Palik [63] and were used as an initial guess for the fit of the ε_d of the Fe layers for all the samples (full, colored lines).

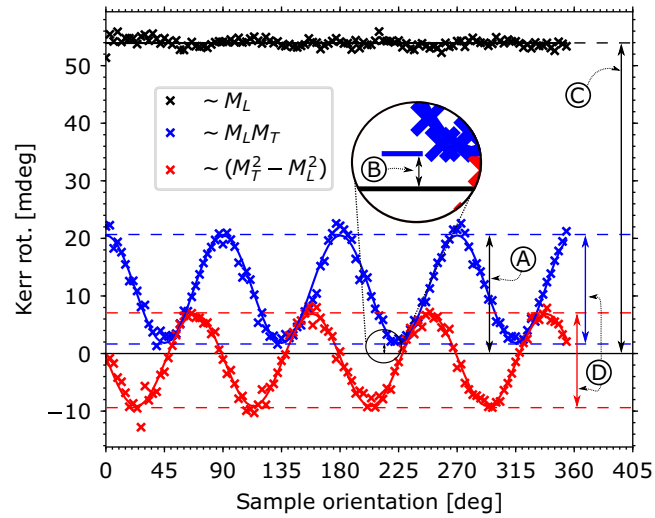

FIG. 6. QMOKE anisotropy measurement at a photon energy of 1.85 eV, with AoI = 45° for the sample with a nominal thickness of 12.5 nm. The dependence of the three MOKE contributions, being LMOKE $\sim M_L$, QMOKE $\sim M_L M_T$ and QMOKE $\sim(M_T^2 - M_L^2)$ on the sample orientation α is demonstrated. Further, several MOKE values are designated in the graph, being Ⓐ $= A_s(2G_{44} - \frac{K^2}{\varepsilon_d})$, Ⓑ $= A_s(G_s - \frac{K^2}{\varepsilon_d})$, Ⓒ $= B_s K$ and Ⓓ $= A_s \Delta G$.

Eqs. (8a)–(8c) shows the outcome of those sequences when using the approximative description of MOKE, Eq. (5), providing selectivity to G_s, $2G_{44}$, and K within validity of Eq. (5), respectively.

The next step is to extract the MO parameters G_s, $2G_{44}$ and K from the measured spectra using the phenomenological description of the MOKE spectra by Yeh's 4×4 matrix formalism [53,61] based on the classical Maxwell equations and boundary conditions. Propagation of coherent electromagnetic plane waves through a multilayer system is considered within this formalism. By solving the wave equation for each layer (characterized by its permittivity tensor and thickness), the reflection matrix $\boldsymbol{R}$ of the multilayer system can be obtained, which allows us to numerically calculate the MOKE angles of the sample according to Eq. (1). The thickness and the ε_d of each layer is known from XRR and ellipsometry measurements, respectively. Nevertheless, the permittivity tensor of the FM layer is described by the sum: $\boldsymbol{\varepsilon} = \boldsymbol{\varepsilon}^{(0)} + \boldsymbol{\varepsilon}^{(1)} + \boldsymbol{\varepsilon}^{(2)}$. Hence, G_s, $2G_{44}$, and K are the unknowns in Yeh's 4×4 matrix formalism calculations, being free parameters to the fit where both measured and calculated sequences are given by Eqs. (8a)–(8c), left side. However, as the measured and calculated spectra are determined by those equal sequences, the determination of spectra of the MO parameters G_s, $2G_{44}$, and K is not affected by an approximation given by Eq. (5). Finally, we would like to point out that the condition of proper positive direction of $\boldsymbol{M}$ rotation angle μ must be met. Although the opposite direction of $\boldsymbol{M}$ rotation will lead only to the opposite sign of experimental spectra, it may lead to completely incorrect spectra of G_s and $2G_{44}$ parameters upon processing. We have checked that all sign conventions as defined in Appendix A agree with experimental procedures, analytical descriptions, and numerical calculations. For further details about this issue, please see Appendix B.

A. Quadratic MOKE anisotropy

The anisotropy of QMOKE is demonstrated by the so-called eight-directional method [10]. The MOKE signal was detected for eight in-plane magnetization directions, being $\mu = 0° + k \times 45°, k = \{0, 1, \ldots, 7\}$. From those measurements, constituent MOKE signals were separated, being namely LMOKE $\sim M_L$ contribution and two quadratic contributions QMOKE $\sim M_L M_T$, and QMOKE $\sim(M_L^2 - M_T^2)$. Note that the separation process could be derived using Eq. (7).

The dependencies of those three MOKE contributions on the sample orientation α are yielded. In Fig. 6, we present all three MOKE contributions measured for the sample with a nominal thickness of 12.5 nm at a photon energy of 1.85 eV and with AoI = 45°. The fourfold anisotropy of the QMOKE contributions and isotropic LMOKE contribution follow the theory well [see α dependence in Eq. (7)]. Note that the separation processes of the contributions $\sim M_L M_T$ for $\alpha = 45°$ and 0° and $\sim M_L$ are identical as described in Eqs. (8a)–(8c), respectively.

B. Linear MOKE spectroscopy

The LinMOKE spectra provide the spectral dependence of K (after processing by Yeh's 4×4 matrix formalism) which is very important for the further QMOKE spectra processing due to the additional K^2/ε_d contribution as follows from Eqs. (8a) and (8b). Also, it is appropriate to provide the complete spectroscopic description of the samples up to the second order in $\boldsymbol{M}$ within this paper.

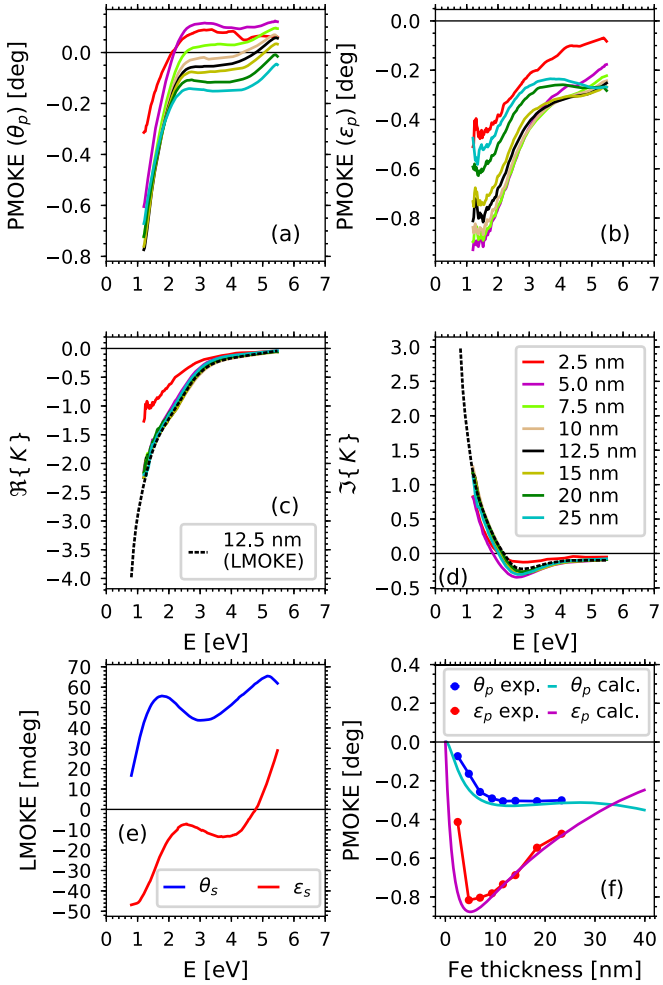

FIG. 7. Experimental PMOKE spectra of (a) Kerr rotation θ_p and (b) Kerr ellipticity ϵ_p at AoI $= 5°$, scaled to magnetization saturation. Spectra of the (c) real and (d) imaginary parts of the MO parameter K yielded from the saturated PMOKE spectra do not differ significantly with the thickness (except for the sample with a nominal thickness of 2.5 nm). The K spectra provided by LMOKE spectroscopy of the sample with a nominal thickness of 12.5 nm agree very well with K spectra obtained from the saturated PMOKE spectra. (e) LMOKE spectra of the sample with a nominal thickness of 12.5 nm. (f) Thickness dependence of PMOKE at a photon energy of 1.85 eV at AoI $= 5°$.

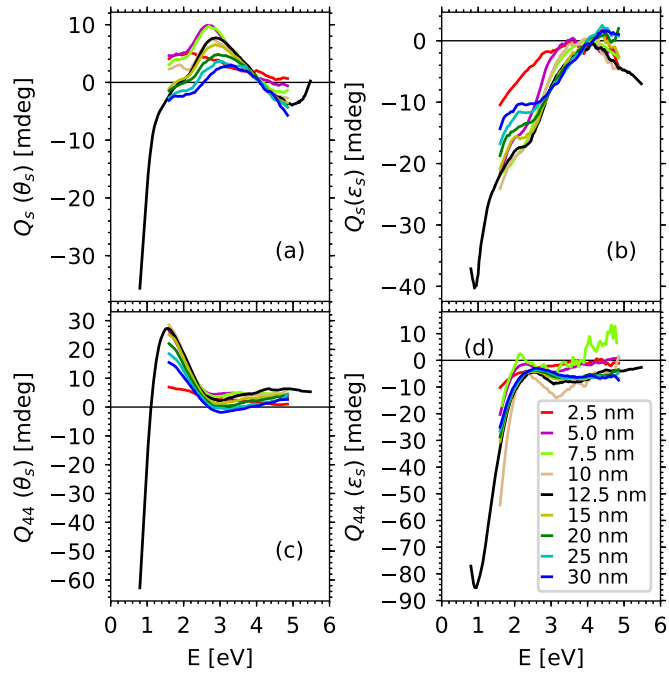

FIG. 8. (a) Rotation and (b) ellipticity of Q_s spectra. (c) Rotation and (d) ellipticity of Q_{44} spectra. All of them measured with s-polarized incident light. The measured spectra were digitally processed (smoothed) with a Savitzky-Golay filter over the photon energy to improve signal-to-noise ratio. The sample with a nominal thickness of 12.5 nm was measured with an extended spectral range of 0.8–5.5 eV. Again, the thinnest sample with a nominal thickness of 2.5 nm shows the largest deviation compared to the other samples of the thickness dependent series.

The PMOKE spectra for all the samples are presented in Figs. 7(a) and 7(b). In Figs. 7(c) and 7(d), we present the K spectra obtained from the PMOKE spectra and in the case of the sample with a nominal thickness of 12.5 nm from the LMOKE spectra, as well. The LMOKE spectra are presented in Fig. 7(e). It should be noted that the PMOKE spectra were measured with the magnetic field of 1.2 T which is not enough to magnetically saturate the samples out of plane. Nevertheless, the PMOKE spectra multiplied by a factor of 2.2 yield spectra in excellent agreement with the K spectra from the LMOKE spectroscopy, both measured on the sample with the nominal thickness of 12.5 nm. We find this excellent agreement as the confirmation of the correctness of the determination of the optical constants of ε_d and K from experimental data. Note that all the presented spectra in the following Sec. VI are recorded only from MOKE measurements with in-plane magnetization, where the samples were always magnetically saturated.

Finally, the dependence of the PMOKE scaled to the magnetization saturation on the Fe layer thickness at a photon energy of 1.85 eV is shown in Fig. 7(f). The experimental data follow the predicted dependence well. All the values that were needed for the Yeh's 4×4 matrix formalism were taken from the sample with a nominal thickness of 12.5 nm and only the thickness of the Fe layer was varied to obtain the thickness dependence [the value of K was provided by LMOKE spectroscopy, hence the experimental value at a nominal thickness of 12.5 nm does not absolutely follow predicted amplitude as one can notice in Fig. 7(f)]. A small disagreement between other experimental and calculated values is due to both slightly different ε_d and K for different Fe thicknesses, as well as a probable small difference in the scaling factor for different Fe layer thicknesses.

C. Quadratic MOKE spectroscopy

The QMOKE spectra for all the samples were measured according to Eqs. (8a) and (8b). The measured spectra in the range of 1.6–4.8 eV are presented in Fig. 8. The sample with a nominal thickness of 12.5 nm was measured at the setup with an extended spectral range of 0.8–5.5 eV. Recall, measured QMOKE also has a contribution from the linear

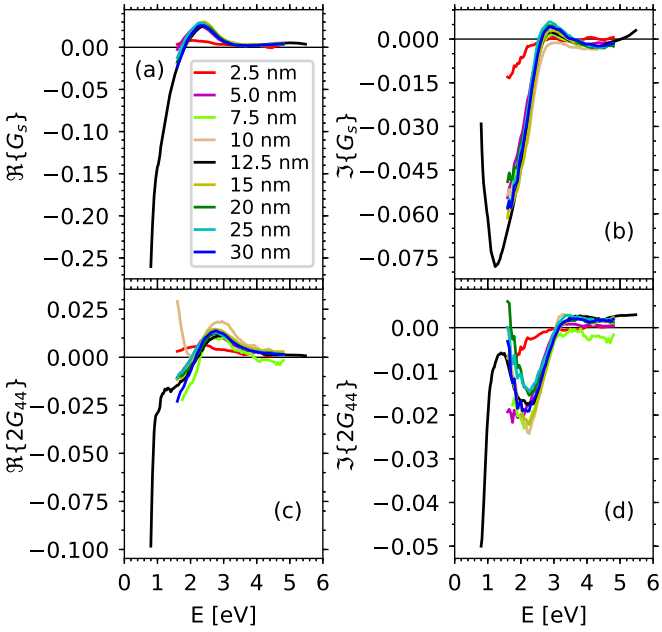

FIG. 9. Spectra of the (a) real and (b) imaginary parts of the quadratic MO parameter G_s and the (c) real and (d) imaginary parts of the quadratic MO parameter $2G_{44}$ for all the samples of the series.

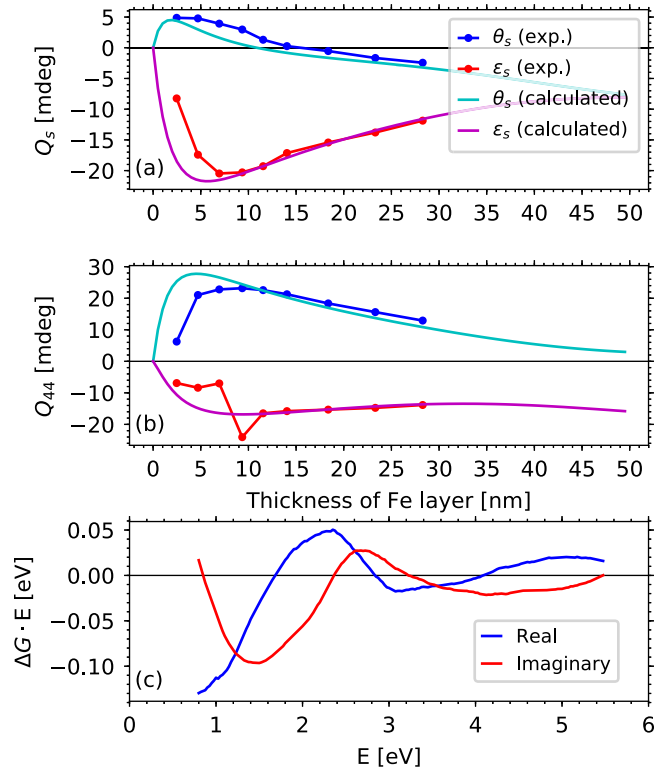

FIG. 10. Thickness dependence of (a) Q_s and (b) Q_{44} for a photon energy of 1.85 eV. Lines were provided by Yeh's 4×4 matrix calculus. Both thickness dependencies are for AoI $= 5°$. (c) The spectral dependence of the real and imaginary part of $\Delta G = G_s - 2G_{44}$ represents the anisotropy strength of the quadratic MO tensor across the whole spectral range. Every point is weighted by its photon energy for clarity.

term K, being proportional to $K^2/\varepsilon_d\, M_L M_T$ provided by cross terms $\varepsilon_{yz}\varepsilon_{zx}/\varepsilon_d$ and $\varepsilon_{zy}\varepsilon_{xz}/\varepsilon_d$ [Eq. (5)]. Let us emphasize, this quadratic-in-magnetization contribution to MOKE arises from optical interplay of two off-diagonal permittivity elements, both being linear in magnetization.

The deduced spectra of the quadratic MO parameters G_s and $2G_{44}$ are shown in Fig. 9. The shape of the spectra do not substantially change with the thickness, showing that there is no substantial contribution from the interface.

The only exception (apart from the sample with a nominal thickness of 2.5 nm, which is also deviating in all previous measurements) is the real part of the $2G_{44}$ spectra below 2 eV for the sample with a nominal thickness of 10 nm. The source of this deviation stems from the interplay of two sources: (i) the ellipticity of Q_{44} spectra is almost twice large in the case of this sample, compared to others [see Fig. 8(d)]. (ii) The value of K is above 1 in spectral range below 2 eV (for both the real and imaginary part, and in the absolute value). Thus the contribution of K^2/ε_d is the dominant contribution to Q_{44} spectra below 2 eV, and therefore a small change in the Q_{44} spectra will substantially affect the yielded $2G_{44}$ spectra.

In Appendix C, we further present a comparison of K, G_s, and $2G_{44}$ spectra of the sample with a nominal thickness of 12.5 nm (prepared by magnetron sputtering) and the sample prepared by MBE. Analogous instability of the $2G_{44}$ parameter can actually be observed here as well. A rather small difference in yielded K spectra and measured Q_{44} spectra provides a significant change of result in yielded $2G_{44}$ spectra. Otherwise, the spectra of samples grown by two different techniques follow the same qualitative progress, but deviate slightly in the magnitude, probably due to small differences in the crystalline quality.

In Figs. 10(a) and 10(b), we present the measured and calculated Fe layer thickness dependence for Q_s and Q_{44}, respectively. The dependence is for a photon energy of 1.85 eV and the calculations are provided by Yeh's 4×4 matrix formalism with AoI $= 5°$ (being the AoI used within the experiment), where ε_d, K, G_s, and $2G_{44}$ were taken from the sample with a nominal thickness of 12.5 nm. The theoretical dependence slightly differs from experimental results for thinner Fe layers. This could be explained by slightly different ε_d, K, G_s, and $2G_{44}$ for the thinner samples as shown in Figs. 5, 7, and 9, respectively, as well as slightly different material properties of capping layers in each sample. Strong deviation could be seen in the case of the experimental value of Q_{44} for the sample with a nominal thickness of 10 nm, as already discussed above.

The parameter $\Delta G = G_s - 2G_{44}$ provides information about the anisotropy strength of the quadratic MO tensor $\boldsymbol{G}$ [40]. Its spectral dependence for the sample with a nominal thickness of 12.5 nm is presented in Fig. 10(c), shown in the form ΔGE, i.e., multiplied by photon energy.

VI. COMPARISON OF EXPERIMENTAL SPECTRA WITH CALCULATIONS AND THE LITERATURE

In this section, we discuss the comparison of experimental spectra with *ab initio* calculations and the literature. All the representative experimental data within this section are from the sample with a nominal Fe thickness of 12.5 nm.

Further, all the spectra in this section are expressed in the form multiplied by photon energy E, being an alternative expression of the conductivity spectra. Note that this is analogous to the well-known relation of conversion between complex permittivity and complex conductivity tensor $\varepsilon_{ij} = \delta_{ij} + i\sigma_{ij}\hbar/(\varepsilon_0 E)$, where E is the photon energy and δ_{ij} the Kronecker delta.

The electronic structure calculations of bcc Fe [69] were performed using the WIEN2K [70] code. The used lattice constant for all calculations was the bulk value, being 2.8665 Å. The electronic structure was calculated for two $\boldsymbol{M}$ directions parallel to Fe[100] and Fe[011], respectively. We used $90^3 = 729\,000$ k points in the full Brillouin zone. The product of the smallest atomic sphere and the largest reciprocal space vector was set to $R_{\mathrm{MT}}K_{\max} = 8$ with the maximum value of the partial waves inside the spheres, $l_{\max} = 10$. The largest reciprocal vector in the charge Fourier expansion was set to $G_{\max} = 12$ Ry$^{1/2}$. The exchange correlation potential LDA was used within all calculations. The convergence criteria were 10^{-6} electrons for charge convergence and 10^{-6} Ry $= 1.4 \times 10^{-5}$ eV for energy convergence. The spin-orbit coupling is included in the second variational method.

The Fermi level was determined by temperature broadened eigenvalues using broadening 0.001 Ry (0.014 eV). The optical properties were determined within electric dipole approximation using the Kubo formula [26,71]. The Drude term (intraband transitions) is omitted in the *ab initio* calculated optical and MO properties. We discuss possibilities of how to handle the Drude contribution in Appendix D. By broadening the spectra and applying the Kramers-Kronig relations, we obtain a full permittivity tensor $\boldsymbol{\varepsilon}$ for each direction of $\boldsymbol{M}$. The spectra for K, G_s, and $2G_{44}$ are obtained directly from the permittivity tensors $\boldsymbol{\varepsilon}$ [72]:

$$K = \tfrac{1}{2}\left(\varepsilon_{yz}^{([100])} - \varepsilon_{zy}^{([100])}\right), \tag{9a}$$

$$G_s = \varepsilon_{xx}^{([100])} - \varepsilon_{yy}^{([100])}, \tag{9b}$$

$$2G_{44} = \varepsilon_{yz}^{([011])} + \varepsilon_{zy}^{([011])}, \tag{9c}$$

where the superscript denotes the $\boldsymbol{M}$ direction in the crystallographic structure.

Figures 11(a) and 11(b) present experimental spectra of $\varepsilon_d - 1$ compared to their *ab initio* calculations. We also present experimental data from the literature [26,66,67] and *ab initio* calculations by Oppeneer *et al.* [26] in the same figure. The imaginary (absorption) part of the diagonal permittivity, $\Im\{\varepsilon_d\}$ is dominated by the absorption peak at 2.4 eV.

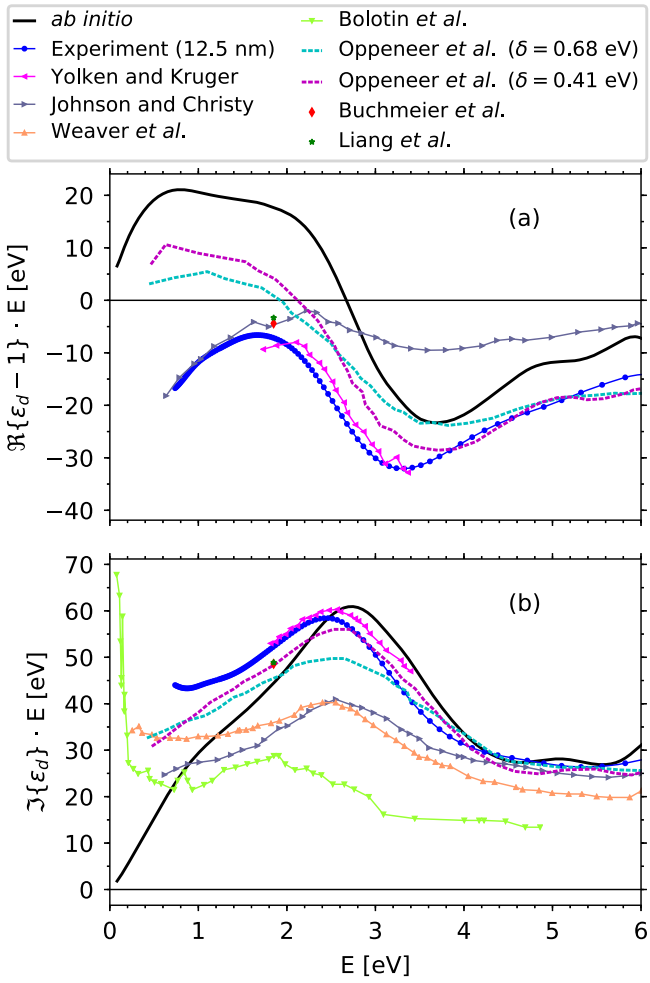

FIG. 11. Experimental (markers) and *ab initio* calculated interband spectra (lines) of (a) real and (b) imaginary parts of $(\varepsilon_d - 1)E$ [eV]. Experimental spectra acquired in this work have marker every ten experimental points (blue bullets). The remaining spectra are taken from literature [26,38,66–68].

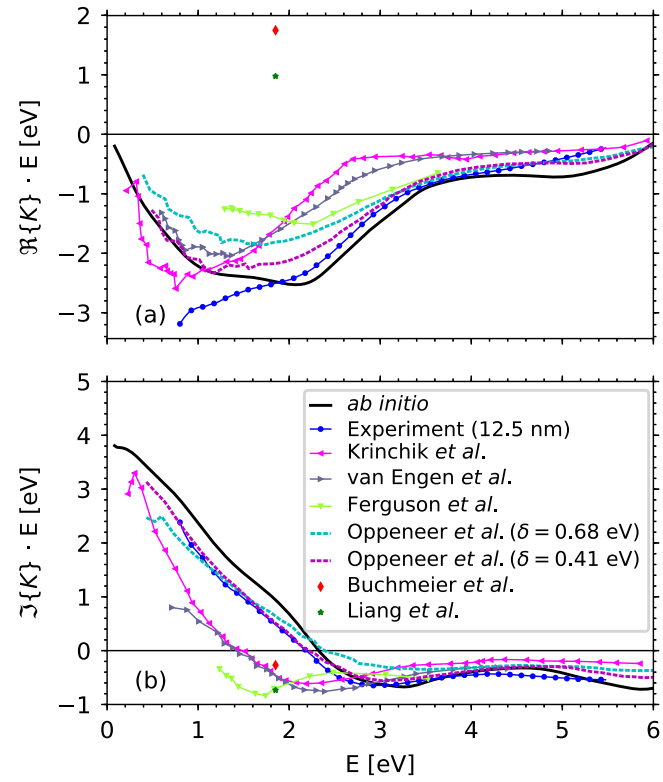

FIG. 12. Experimental (markers) and *ab initio* calculated interband spectra (lines) of the (a) real and (b) imaginary parts of KE [eV]. Experimental spectra acquired in this work have a marker every five experimental points (blue bullets). The remaining spectra are taken from the literature [24–26,38,68].

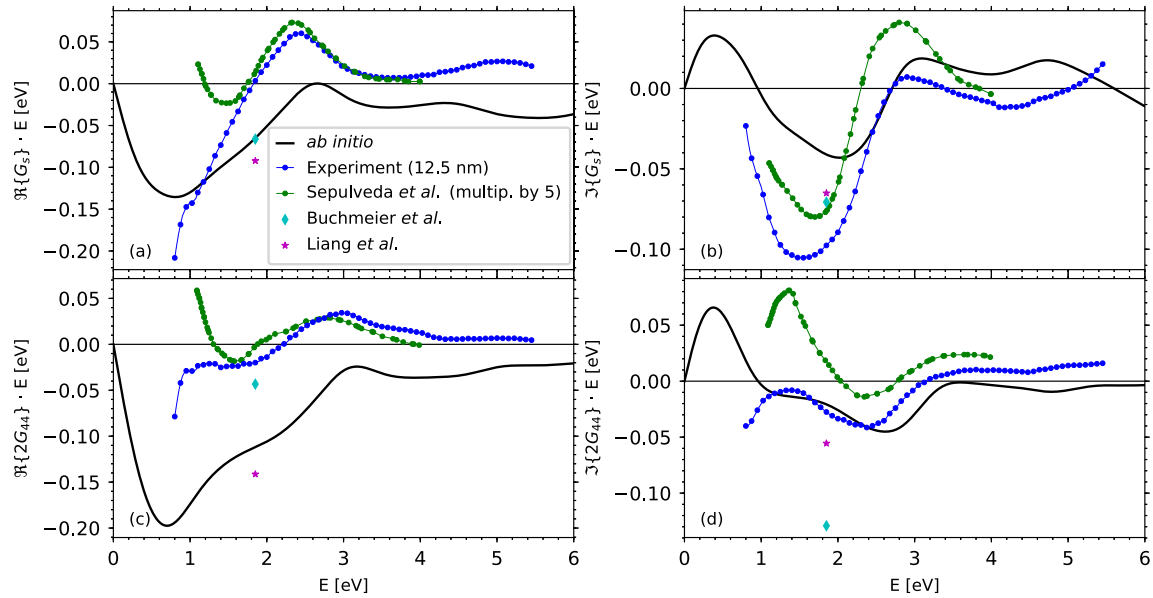

FIG. 13. The experimental G_s spectra [(a) and (b)] and the experimental $2G_{44}$ spectra [(c) and (d)] compared with the *ab initio* calculations. G_s spectra are calculated for $\vec{M} \parallel [100]$ and $2G_{44}$ spectra calculated for $\vec{M} \parallel [011]$ both with smearing of FWHM = 1.2 eV and with $90^3 = 729\,000$ k points in the full Brillouin zone. Further, we show a comparison with data taken from the literature [36,38,68]. The spectra taken from Sepúlveda *et al.* [36] have been multiplied by a factor of 5 to be comparable with our experimental spectra.

This peak originates from transitions of mostly 3*d* down electrons above and below the Fermi level. The *ab initio* calculated peak position is very stable regarding small changes of the lattice constant, magnetization direction, and small distortion of the Fe lattice. On the other hand, the peak position is determined by the selected exchange potential, where LDA provides the closest match to the experimental results, while other potentials (GGA, LDA + U, GGA + U) display larger deviation from the experimental peak position. Therefore we choose the LDA exchange potential to calculate the electronic structure of bcc Fe, although LDA still overestimates the width of the occupied 3*d* bands. The width of the occupied 3*d* bands can be corrected using dynamical mean-field theory (DMFT) [73]. Further, note that the peak amplitude depends on the smearing parameter [26], and we chose smearing $\delta = 0.6$ eV in the case of ε_d to adjust the peak height.

Figures 12(a) and 12(b) show a comparison between experimental and *ab initio* calculated spectra of K, demonstrating excellent agreement. Note the absorption part corresponds to $\Re\{K\}$, with two peaks at 2.0 and 1.1 eV. The amplitude of $\Re\{KE\}$ is about −2.5 eV, i.e., about 4% of the maximal value of $\Im\{\varepsilon_d E\}$ being about 60 eV. Although in both figures (Figs. 11 and 12) absolute values differ by dozens of percent for some photon energies, the peaks and courses of spectra, being characteristic for the given material, are very similar for all the presented data, both experimental and theoretical (note that disagreement with the reported values at single wavelength [38,68] is probably due to sign inconsistency). Further, the dc limit of the imaginary part of the K spectra corresponds to the anomalous Hall conductivity. Its value extracted from the *ab initio* calculation is 512 $(\Omega\ \mathrm{cm})^{-1}$ [760 $(\Omega\ \mathrm{cm})^{-1}$ without broadening] agreeing with the value provided in Ref. [74]. Finally, note that sign of *ab initio* (WIEN2K ver. 17) calculated K spectra is reversed, to agree with the sign of the experimental K spectra (this sign error was corrected in WIEN2K ver. 19.1).

Figure 13 shows experimental spectra of the real (a) and imaginary (b) parts of G_s spectra, compared with the *ab initio* calculations. The fundamental (imaginary) part of G_s has a pronounced peak at 1.6 eV with the amplitude in the experimental spectra being $\Im\{G_s E\} = -0.11$ eV. The main features of G_s are well-described by *ab initio* spectra. However, the *ab initio* calculated peak at 1.6 eV has about half that amplitude. Figures 13(c) and 13(d) show the real and imaginary parts of the experimental spectra of $2G_{44}$, respectively, compared to the *ab initio* calculations. In the case of the fundamental part of $2G_{44}$ spectra, both shape and amplitude are well described *ab initio*. The larger disagreement between $\Re\{G_s\}$, $\Re\{2G_{44}\}$ and their *ab initio* descriptions (particularly for small photon energies) could be due to the missing Drude term, which is omitted in the *ab initio* calculations, and which mainly contributes to the real part of the permittivity at small photon energies. Finally, note that in the *ab initio* calculations, convergence (for example, on density of the k mesh) of $2G_{44}$ is much better compared to G_s, as G_s is calculated as a small change of the diagonal permittivities [Eq. (9b)], whereas $2G_{44}$ is calculated from off-diagonal permittivity [Eq. (9c)].

Further, we show the comparison of the spectral dependence of G_s and $2G_{44}$ from Sepúlveda *et al.* [36]. The spectra had to be multiplied by a factor of 5 to be comparable to our experimental and the *ab initio* spectra. Then, the agreement is perfect for the real part of both G_s and $2G_{44}$ in the spectral range 1.5–4.0 eV. The disagreement of spectral dependence under 1.5 eV can be explained by different sample quality; as the same behavior was already experienced for $2G_{44}$ in the case of the sample with a nominal thickness of 10 nm and also in the case of the sample prepared by MBE, which is discussed in a previous Sec. V C and in Appendix C, respectively. The

comparison of the imaginary part of G_s and $2G_{44}$ between our data and the scaled data of Sepúlveda *et al.* [36] provide very similar behavior except for some offset and also different amplitude of peaks, especially in case of the $\Im\{2G_{44}\}$ peak at 1.5 eV. We do not know wherefrom the scaling factor 5 between our data and data of Sepúlveda *et al.* is stemming. In the case of Sepúlveda *et al.,* the data were obtained from experimental measurement of variation of reflectivity with quadratic dependence on magnetization. The poor quality of the samples can be ruled out, as in the case of polycrystalline material $\Delta G = 0$, i.e., $G_s = 2G_{44}$, which is not the case here. However, note that our optical spectra of ε_d, K, $2G_{44}$, and G_s well describe their experimental reflectivity spectra using our numerical model.

Finally, the supplemental data files in Ref. [75] provide spectra of ε_d, K, G_s, and $2G_{44}$, being the experimental spectra of the sample with a nominal thickness of 12.5 nm, where the spectra are expressed in the form of the permittivity (i.e., the spectra are not in the form multiplied by its photon energy). Further data sets can be received upon request.

VII. CONCLUSION

We provided a detailed description of our approach to the QMOKE spectroscopy, which allows us to obtain quadratic MO parameters in the extended visible spectral range. The experimental technique stems from the eight-directional method that separates LinMOKE and QMOKE contributions.

The quadratic MO parameters G_s and $2G_{44}$ of bcc Fe (expressing magnetic linear dichroism of permittivity along the [100] and [110] directions, respectively) were systematically investigated. The spectral dependence of G_s and $2G_{44}$ is experimentally determined in the spectral range 0.8–5.5 eV, being acquired by QMOKE spectroscopy and numerical simulations using Yeh's 4×4 matrix formalism. A sample series of Fe thin films with varying thicknesses grown by magnetron sputtering on MgO(001) substrates and capped with 2.5 nm of silicon were used. Except for the sample with a nominal thickness of 2.5 nm, the dependence of the obtained spectra on the Fe layer thickness is small, indicating a small contribution of the interface. During our investigations, the linear MO parameter K in the spectral range 0.8–5.5 eV and the diagonal permittivity ε_d in the spectral range 0.7–6.4 eV were also acquired.

Further, all measured permittivity spectra are compared to *ab initio* calculations. The shapes of those spectra are well described by electric dipole approximation, with the electronic structure of bcc Fe calculated using DFT with LDA exchange-correlation potential and with spin-orbit coupling included. However, to describe G_s and $2G_{44}$, a fine mesh of $90 \times 90 \times 90$ is used as G_s is calculated as a small variation of diagonal permittivity ε_{ii} with magnetization direction.

With the measurement process well established, the technique is ready to be used on other ferromagnetic materials, and also tested on antiferromagnetic materials. A suitable candidate could be the easy-plane AFM NiO grown on a ferri- or ferromagnetic support in order to control the AFM by the exchange coupling to the additional ferri- or ferromagnetic layer which can be magnetically aligned by an external field. In such a bilayer, the contribution of the ferri- or ferromagnetic layer has to be studied separately in the same manner as we have done here for bcc Fe.

ACKNOWLEDGMENTS

The authors thank Günter Reiss, Jaromír Pištora, Gerhard Götz, Karel Výborný, and John Cawley for support, assistance and discussion. This work was supported by Czech Science Foundation (19-13310S) and the Deutsche Forschungsgemeinschaft (DFG Re 1052/37-1). The work was also supported by the European Regional Development Fund through the IT4Innovations National Supercomputing Center-path to exascale project, project No. CZ. 02.1.01/0.0/0.0/16_013/0001791 within the Operational Programme Research, Development and Education and supported in part by OP VVV project MATFUN under Grant CZ.02.1.01/0.0/0.0/15_003/0000487.

APPENDIX A: SIGN CONVENTIONS

Within the fields of optics and MO, there is a vast amount of conventions. As there is no generally accepted system of conventions, we define here all conventions adopted within this work.

To describe reflection from a sample, three Cartesian systems are needed, one for incident light beam, one for reflected light beam and one for the sample. All those Cartesian systems are right-handed and defined in Fig. 1 of the main text.

Time convention. The electric field vector of an electromagnetic wave is described by negative time convention as $\boldsymbol{E}(\boldsymbol{r}, t) = \boldsymbol{E}(\boldsymbol{r})e^{-i\omega t}$, providing permittivity in the form $\varepsilon = \Re\{\varepsilon\} + i\Im\{\varepsilon\}$, where the imaginary part of complex permittivity $\Im\{\varepsilon\} > 0$.

Cartesian referential of the sample. The Cartesian system describing the sample is the right-handed $\hat{x}, \hat{y}, \hat{z}$ system, where $\hat{z}$ axis is normal to the surface of the sample, and points into the sample. The $\hat{y}$ axis is parallel with the plane of light incidence and with the sample surface, while its positive direction is defined by the direction of k_y, being the $\hat{y}$ component of the wave vector of incident light as shown in Fig. 1. In this system, rotations of the crystallographic structure and magnetization take place.

Cartesian referential of light. We use the right-handed Cartesian system $\hat{s}$, $\hat{p}$, $\hat{k}$ for description of the incident and reflected light beam. The direction of vector $\hat{k}$ defines the direction of propagation of light. Vector $\hat{p}$ lies in the incident plane, i.e., a plane defined by incident and reflected beam. The vector $\hat{s}$ is perpendicular to this plane and corresponds to $\hat{x}$. This convention is the same for both incident and reflected beams (Fig. 1).

Convention of the Kerr angles. The Kerr rotation θ is positive if azimuth θ of the polarization ellipse rotates clockwise, when looking into the incoming light beam. The Kerr ellipticity ϵ is positive if temporal evolution of the electric field vector $\boldsymbol{E}$ rotates clockwise when looking into the incoming light beam.

Convention of rotation of the sample, the magnetization, and the optical elements. The rotation is defined as positive if the rotated vector pointing in the $\hat{x}$ ($\hat{s}$) direction rotates towards the $\hat{y}$ ($\hat{p}$) direction. The sample orientation $\alpha = 0$

corresponds to the Fe[100] direction being parallel to the $\hat{x}$ axis and, when looking at the top surface of the sample, the positive rotation of the sample is clockwise. Likewise, the magnetization direction $\mu = 0$ corresponds to $\boldsymbol{M}$ being in the positive direction of the $\hat{x}$ axis and, when looking at the top surface of the sample, the positive rotation of magnetization $\boldsymbol{M}$ is clockwise. Further, when looking into the incoming beam, the positive rotation of the optical elements is counterclockwise, in contrast to the positive Kerr angles, defined by historical convention.

APPENDIX B: CONSEQUENCES OF THE MOKE SIGN DISAGREEMENT BETWEEN THE EXPERIMENTAL AND NUMERICAL MODELS

The correct sign of LMOKE and QMOKE spectra is given by the conventions used. Nevertheless, to obtain the correct spectra of MO parameters K, G_s, and $2G_{44}$, the same conventions must be adopted within the numerical model and the experiment. One would intuitively expect only the reversed sign of yielded MO parameters, when the sign conventions of the experiment and the numerical model do not comply. However, completely incorrect values are yielded in this case for the quadratic MO parameters.

There are numerous points in the experiment where we can go wrong and thus measure the MOKE spectra of the incorrect sign according to our conventions, e.g., wrong direction of in-plane $\boldsymbol{M}$ rotation (i.e., $\mu \to -\mu$), wrong direction of positive external field and thus opposite direction of $\boldsymbol{M}$ (i.e., $\mu \to \mu + 180°$), error in the calibration process of the setup itself (note that the positive direction of the optical element rotation and the positive direction of the Kerr rotation have opposite conventions) or some quirk in the processing algorithm of the measured data itself (usually we measure change of intensity, which has to be converted to Kerr angles). Further, we can also make a sign error in the code of the numerical model.

The correct sign of the numerical model output can be checked for by comparison to the simple analytic model that exist for some special cases. For example, PMOKE effect Φ at the normal angle of incidence for a vacuum/FM(bulk) interface within our sign convention:

$$\Phi = \frac{\varepsilon_{xy}}{\sqrt{\varepsilon_d^{(\mathrm{FM})}}\left(1 - \varepsilon_d^{(\mathrm{FM})}\right)}. \tag{B1}$$

Various sign mistakes in the experiment will not always lead to the same error, e.g., the wrong direction of positive external magnetic field will affect the sign of LMOKE spectra but not the QMOKE spectra. On the other hand the wrong direction of $\boldsymbol{M}$ rotation will produce a wrong sign of both spectra, LMOKE and QMOKE alike—see the Eqs. (8a)–(8c).

In the following, we will discuss a consequence of the latter case, when the direction of $\boldsymbol{M}$ rotation has the opposite direction, $\mu' \to -\mu$ leading to a wrong sign of experimental spectra measured according to Eqs. (8a)–(8c). While linear MO parameter K', yielded from the LMOKE spectra with a reversed sign, will only have the opposite sign compared to the true MO parameter K, the quadratic MO parameters G_s' and $2G_{44}'$, yielded from the Q_s and Q_{44} spectra with the opposite sign, will be completely different from the true MO parameters G_s and $2G_{44}$, respectively. This is due to the contribution of K^2/ε_d to the Q_s and Q_{44} spectra, which are invariant to the sign of K itself. Thus the MO parameters yielded from sign-reversed experimental spectra are bound with the true MO parameters by the equations:

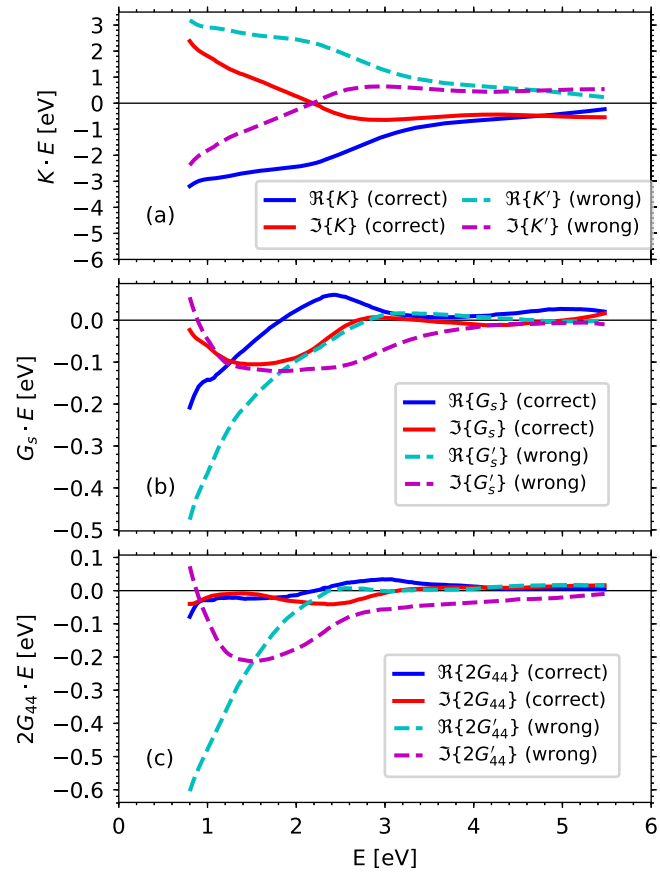

FIG. 14. Comparison of the spectra of MO parameters of (a) K, (b) G_s, and (c) $2G_{44}$ to the MO parameters yielded from the experimental spectra with the wrong (reversed) sign of μ (K', G_s', and $2G_{44}'$).

$$K' = -K, \tag{B2}$$

$$G_s' = -G_s + 2\frac{K^2}{\varepsilon_d}, \tag{B3}$$

$$2G_{44}' = -2G_{44} + 2\frac{K^2}{\varepsilon_d}. \tag{B4}$$

In Fig. 14, we show the wrong MO parameters K', G_s', and $2G_{44}'$ compared to the true MO parameters K, G_s, and $2G_{44}$.

Note that neither the shape nor the sign of the true MO parameters is given by the convention used. Any sign conventions can be adopted, but the crucial point is that the conventions used in real experiments and in numerical calculus are the same. Obviously, this issue applies to any error in the experimental setup or the numerical code that would unintentionally reverse the sign of the measured or calculated MOKE spectra, respectively.

APPENDIX C: COMPARISON OF THE SAMPLES GROWN BY MOLECULAR BEAM EPITAXY AND BY MAGNETRON SPUTTERING

Fe and Si films were prepared on a single-crystalline MgO(001) substrate via MBE. Prior to deposition, the substrates were annealed at 400 °C for 1 h in a 1×10^{-4} mbar oxygen atmosphere to remove carbon contamination and obtain defined surfaces. Fe films were deposited by thermal evaporation from a pure metal rod at a substrate temperature of 250 °C. Silicon capping layers were evaporated at room temperature using a crucible. The deposition rates of 1.89 and 0.3 nm/min for Fe and Si, respectively, were used and controlled by a quartz microbalance next to the source. The base pressure in the UHV chamber was 10^{-8} mbar.

The XRD and XRR were measured as described in Sec. III. A thickness of 12.6 nm was determined by XRR for the MBE prepared Fe layer and 7.0 nm for the $Si + SiO_x$ capping layer. The thickness of the reference sample with only $Si + SiO_x$ capping was 8.1 nm. The XRD Θ-2Θ scan was performed around $2\Theta = 65^\circ$ and showed that the samples are of good crystallinity. Further, the ellipsometry, LMOKE and QMOKE spectroscopy were measured on the sample to feed the Yeh's 4×4 matrix calculations with the required sample data. The spectra of K, G_s, and $2G_{44}$ obtained by numerical calculations are presented and compared to the spectra of the sputter-deposited sample with a nominal thickness of 12.5 nm in Figs. 15(a)–15(c), respectively. The behavior of the spectra of both samples is very similar, except for the real part of $2G_{44}$ spectra at lower photon energies. Nevertheless the same discrepancy has already been discussed in Sec. V C for the case of the 10-nm sample. Otherwise the differences of absolute values across spectra are not surprising, as the reported experimental values of MO parameters differ for different samples prepared by different deposition techniques and different groups (as shown in Figs. 11–13), probably being connected with slightly different crystalline qualities of the Fe layer.

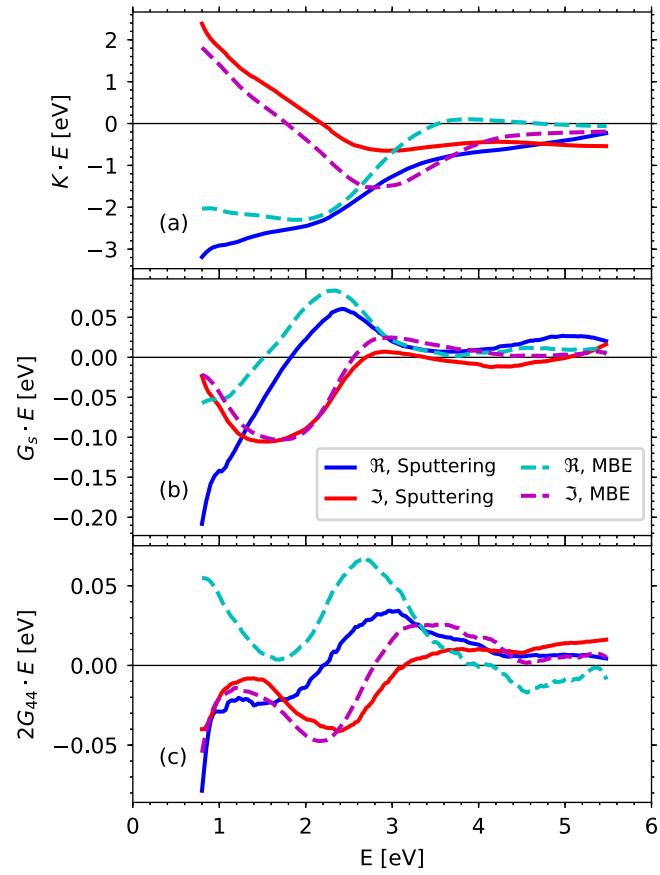

FIG. 15. Comparison of the spectra of the MO parameters of (a) K, (b) G_s, and (c) $2G_{44}$ of two samples, one prepared by magnetron sputtering and the other by MBE. For each of the samples, all the data used within numerical calculations were obtained from the parameters of the particular sample.

APPENDIX D: THE DRUDE CONTRIBUTION

The contribution of intraband transitions in the diagonal permittivity could be described by the classical phenomenological Lorentz-Drude model (in the following, called the Drude term)

$$\varepsilon_D = 1 - \frac{E_p^2}{E^2 + i\Gamma E}, \tag{D1}$$

where E is the photon energy, $E_p = \hbar\omega_p$ is the plasma energy describing the strength of the oscillator, with ω_p being the plasma frequency and $\Gamma = \hbar\tau^{-1}$ the damping constant, and 1 stands for the relative vacuum permittivity.

In order to include the Drude term into G spectra, first recall that G_s and $2G_{44}$ express MLD, $G_s = \varepsilon_\parallel - \varepsilon_\perp$ for $\boldsymbol{M} \parallel \langle 100\rangle$ and $2G_{44} = \varepsilon_\parallel - \varepsilon_\perp$ for $\boldsymbol{M} \parallel \langle 110\rangle$ where parallel ($\parallel$) and perpendicular ($\perp$) denote the direction of the applied electric field (i.e., linear light polarization) with respect to the magnetization direction. Second, we assume both $\varepsilon_\parallel$ and $\varepsilon_\perp$ are described by the Drude model (D1), however, with plasma energy E_p and damping constant Γ slightly different for both $\parallel$ and $\perp$ directions

$$\begin{aligned}\mathrm{MLD}_D = \varepsilon_\parallel - \varepsilon_\perp &= \Delta E_p \frac{\partial}{\partial E_p}\varepsilon_D + \Delta\Gamma \frac{\partial}{\partial \Gamma}\varepsilon_D \\ &= \varepsilon_D\left[\frac{2\Delta E_p}{E_p} - \frac{i\Delta\Gamma}{-E + i\Gamma}\right],\end{aligned} \tag{D2}$$

where MLD_D denotes the Drude contribution to MLD, with $\Delta E_p = E_{p,\parallel} - E_{p,\perp}$ and $\Delta\Gamma = \Gamma_\parallel - \Gamma_\perp$ being differences of the plasma energy and the damping constant between parallel and perpendicular magnetization directions, respectively. Due to the anisotropy of G spectra, ΔE_p and $\Delta\Gamma$ have different values for $\boldsymbol{M} \parallel \langle 100\rangle$ and $\boldsymbol{M} \parallel \langle 110\rangle$.

The number of free parameters in the Eqs. (D1) and (D2) can be reduced from four to two if values of dc conductivity and AMR are known. One part of the sample with a nominal thickness of 12.5 nm was patterned into a Hall bar with a top down process using UV lithography and Argon milling. Four point conductivity measurements were performed for various applied currents in the [100] direction from 50 to 500 μA. The characteristic dimensions of the Hall bar are length = 635 μm, width = 80 μm, and height = 11.5 nm. The resistivity, and thus the conductivity, was determined by performing a linear fit to the data. One obtains conductivity values of $\sigma_\parallel =$

0.4002×10^7 S/m and $\sigma_\perp = 0.4020 \times 10^7$ S/m, being the conductivity with $\boldsymbol{M}$ parallel and perpendicular to the current, respectively. The AMR value of 0.45% correspond well with the literature [76].

The conductivity σ and relative permittivity ε are related by $(\varepsilon - 1)\varepsilon_0 = i\sigma\hbar/E$, where ε_0 is the vacuum permittivity and $\hbar$ is the reduced Planck constant. Hence, at $E = 0$, dc conductivity is

$$\sigma = \frac{\varepsilon_0}{\hbar}\frac{E_p^2}{\Gamma} \tag{D3}$$

and the (dc) anisotropy magnetoresistance is

$$\mathrm{AMR} = \sigma_\perp - \sigma_\parallel = \frac{\varepsilon_0}{\hbar}\lim_{E\to 0}\left[iE(\varepsilon_\parallel - \varepsilon_\perp)\right]$$

$$= \sigma\left[\frac{2\Delta E_p}{E_p} - \frac{\Delta\Gamma}{\Gamma}\right]. \tag{D4}$$

In order to discuss the Drude contribution to G_s and $2G_{44}$, we first determine the Drude contribution to $(\varepsilon_d - 1)$. Knowing the experimental value of dc conductivity and fitting the Drude model of Eqs. (D3) and (D1) to the difference between experimental and interband (i.e., *ab initio*) spectra, the only free parameter in the fit is the plasma frequency becoming $E_p = 4.95$ eV and the corresponding damping term $\Gamma = 0.082$ eV. Further, we use the experimental value of dc AMR. Recall, AMR was measured solely for current in [100], i.e., for determination of the Drude contribution to G_s. However, we can assume an equal experimental Drude contribution also for the current in the [110] direction when estimating the Drude contribution to $2G_{44}$. Then, combining Eqs. (D2) and (D4), $\Delta\Gamma$ can be eliminated resulting in only one free parameter ΔE_p to describe the Drude contribution to G_s and $2G_{44}$ spectra.

[1] T. Jungwirth, X. Marti, P. Wadley, and J. Wunderlich, Antiferromagnetic spintronics, Nat. Nanotechnol. **11**, 231 (2016).

[2] P. Wadley, B. Howells, J. Železný, C. Andrews, V. Hills, R. P. Campion, V. Novák, K. Olejník, F. Maccherozzi, S. S. Dhesi, S. Y. Martin, T. Wagner, J. Wunderlich, F. Freimuth, Y. Mokrousov, J. Kuneš, J. S. Chauhan, M. J. Grzybowski, A. W. Rushforth, K. W. Edmonds, B. L. Gallagher, and T. Jungwirth, Electrical switching of an antiferromagnet, Science **351**, 587 (2016).

[3] J. Kerr, On rotation of the plane of polarization by reflection from the pole of a magnet, Philos. Mag. **3**, 321 (1877).

[4] P. Němec, M. Fiebig, T. Kampfrath, and A. V. Kimel, Antiferromagnetic opto-spintronics, Nat. Phys. **14**, 229 (2018).

[5] S. Baierl, M. Hohenleutner, T. Kampfrath, A. K. Zvezdin, A. V. Kimel, R. Huber, and R. V. Mikhaylovskiy, Nonlinear spin control by terahertz-driven anisotropy fields, Nat. Photonics **10**, 715 (2016).

[6] A. V. Kimel, B. A. Ivanov, R. V. Pisarev, P. A. Usachev, A. Kirilyuk, and T. Rasing, Inertia-driven spin switching in antiferromagnets, Nat. Phys. **5**, 727 (2009).

[7] T. Kampfrath, A. Sell, G. Klatt, A. Pashkin, S. Mährlein, T. Dekorsy, M. Wolf, M. Fiebig, A. Leitenstorfer, and R. Huber, Coherent terahertz control of antiferromagnetic spin waves, Nat. Photonics **5**, 31 (2011).

[8] V. Saidl, P. Němec, P. Wadley, V. Hills, R. P. Campion, V. Novák, K. W. Edmonds, F. Maccherozzi, S. S. Dhesi, B. L. Gallagher, F. Trojánek, J. Kuneš, J. Železný, P. Malý, and T. Jungwirth, Optical determination of the Néel vector in a CuMnAs thin-film antiferromagnet, Nat. Photonics **11**, 91 (2017).

[9] Š. Višňovský, Magneto-Optical Permittivity tensor in crystals, Czech. J. Phys. B **36**, 1424 (1986).

[10] K. Postava, D. Hrabovský, J. Pištora, A. R. Fert, Š. Višňovský, and T. Yamaguchi, Anisotropy of quadratic magneto-optic effects in reflection, J. Appl. Phys. **91**, 7293 (2002).

[11] N. Kanda, T. Higuchi, H. Shimizu, K. Konishi, K. Yoshioka, and M. Kuwata-Gonokami, The vectorial control of magnetization by light, Nat. Commun. **2**, 362 (2011).

[12] T. Higuchi and M. Kuwata-Gonokami, Control of antiferromagnetic domain distribution via polarization-dependent optical annealing, Nat. Commun. **7**, 10720 (2016).

[13] G. R. Hoogeboom, A. Aqeel, T. Kuschel, T. T. M. Palstra, and B. J. van Wees, Negative spin Hall magnetoresistance of Pt on the bulk easy-plane antiferromagnet NiO, Appl. Phys. Lett. **111**, 052409 (2017).

[14] W. Lin and C. L. Chien, Electrical Detection of Spin Backflow from an Antiferromagnetic Insulator $Y_3Fe_5O_{12}$ Interface, Phys. Rev. Lett. **118**, 067202 (2017).

[15] D. Hou, Z. Qiu, J. Barker, K. Sato, K. Yamamoto, S. Vélez, J. M. Gomez-Perez, L. E. Hueso, F. Casanova, and E. Saitoh, Tunable Sign Change of Spin Hall Magnetoresistance in Pt/NiO/YIG Structures, Phys. Rev. Lett. **118**, 147202 (2017).

[16] J. Hamrle, S. Blomeier, O. Gaier, B. Hillebrands, H. Schneider, G. Jakob, B. Reuscher, A. Brodyanski, M. Kopnarski, K. Postava, and C. Felser, Ion beam induced modification of exchange interaction and spin-orbit coupling in the Co_2FeSi Heusler compound, J. Phys. D: Appl. Phys. **40**, 1558 (2007).

[17] J. Hamrle, S. Blomeier, O. Gaier, B. Hillebrands, H. Schneider, G. Jakob, K. Postava, and C. Felser, Huge quadratic magneto-optical Kerr effect and magnetization reversal in the Co_2FeSi Heusler compound, J. Phys. D: Appl. Phys. **40**, 1563 (2007).

[18] P. K. Muduli, W. C. Rice, L. He, and F. Tsui, Composition dependence of magnetic anisotropy and quadratic magnetooptical effect in epitaxial films of the Heusler alloy Co_2MnGe, J. Magn. Magn. Mater. **320**, L141 (2008).

[19] P. K. Muduli, W. C. Rice, L. He, B. A. Collins, Y. S. Chu, and F. Tsui, Study of magnetic anisotropy and magnetization reversal using the quadratic magnetooptical effect in epitaxial $Co_xMn_yGe_z(111)$ films, J. Phys.: Condens. Matter **21**, 296005 (2009).

[20] S. Trudel, J. Hamrle, B. Hillebrands, T. Taira, and M. Yamamoto, Magneto-optical investigation of epitaxial nonstoichiometric Co_2MnGe thin films, J. Appl. Phys. **107**, 043912 (2010).

[21] S. Trudel, G. Wolf, J. Hamrle, B. Hillebrands, P. Klaer, M. Kallmayer, H. J. Elmers, H. Sukegawa, W. Wang, and K. Inomata, Effect of annealing on $Co_2FeAl_{0.5}Si_{0.5}$ thin films: A magneto-optical and x-ray absorbtion study, Phys. Rev. B **83**, 104412 (2011).

[22] O. Gaier, J. Hamrle, S. J. Hermsdoerfer, H. Schultheiss, B. Hillebrands, Y. Sakuraba, M. Oogane, and Y. Ando, Influence of the $L2_1$ ordering degree on the magnetic properties of Co_2MnSi Heusler films, J. Appl. Phys. **103**, 103910 (2008).

[23] G. Wolf, J. Hamrle, S. Trudel, T. Kubota, Y. Ando, and B. Hillebrands, Quadratic magneto-optical Kerr effect in Co_2MnSi, J. Appl. Phys. **110**, 043904 (2011).

[24] P. E. Ferguson and R. J. Romagnoli, Transverse kerr magneto-optic effect and optical properties of transition-rare-earth alloys, J. Appl. Phys. **40**, 1236 (1969).

[25] G. S. Krinchik and V. A. Artemjev, Magneto-optic properties of nickel, iron, and cobalt, J. Appl. Phys. **39**, 1276 (1968).

[26] P. M. Oppeneer, T. Maurer, J. Sticht, and J. Kübler, *Ab initio* calculated magneto-optical Kerr effect of ferromagnetic metals: Fe and Ni, Phys. Rev. B **45**, 10924 (1992).

[27] Š. Višňovský, M. Nývlt, V. Prosser, R. Lopušník, R. Urban, J. Ferré, G. Pénissard, D. Renard, and R. Krishnan, Polar magneto-optics in simple ultrathin-magnetic-film structures, Phys. Rev. B **52**, 1090 (1995).

[28] S. Uba, L. Uba, A. N. Yaresko, A. Ya. Perlov, V. N. Antonov, and R. Gontarz, Optical and magneto-optical properties of Co/Pt multilayers, Phys. Rev. B **53**, 6526 (1996).

[29] Š. Višňovský, R. Lopušník, M. Nývlt, A. Das, R. Krishnan, M. Tessier, Z. Frait, P. Aitchison, and J. N. Chapman, Magneto-optic studies of Fe/Au multilayers, J. Magn. Magn. Mater. **198-199**, 480 (1999).

[30] K. H. J. Buschow, *Handbook of Magnetic Materials* (Elsevier Science B. V., Amsterdam, The Netherlands, 2001), Vol. 13.

[31] J. Hamrle, M. Nývlt, Š. Višňovský, R. Urban, P. Beauvillain, R. Mégy, J. Ferré, L. Polerecký, and D. Renard, Magneto-optical properties of ferromagnetic/nonferromagnetic interfaces: Application to Co/Au(111), Phys. Rev. B **64**, 155405 (2001).

[32] J. Hamrle, J. Ferré, M. Nývlt, and Š. Višňovský, In-depth resolution of the magneto-optical Kerr effect in ferromagnetic multilayers, Phys. Rev. B **66**, 224423 (2002).

[33] J. Gřondilová, M. Rickart, J. Mistrík, K. Postava, Š. Višňovský, T. Yamaguchi, R. Lopušník, S. O. Demokritov, and B. Hillebrands, Anisotropy of magneto-optical spectra in ultrathin Fe/Au/Fe bilayers, J. Appl. Phys. **91**, 8246 (2002).

[34] Š. Višňovský, M. Veis, E. Lišková, V. Kolinský, P. D. Kulkarni, N. Venkataramani, S. Prasad, and R. Krishnan, MOKE spectroscopy of sputter-deposited Cu-ferrite films, J. Magn. Magn. Mater. **290-291**, 195 (2005).

[35] M. Veis, L. Beran, R. Antoš, D. Legut, J. Hamrle, J. Pištora, C. Sterwerf, M. Meinert, J.-M. Schmalhorst, T. Kuschel, and G. Reiss, Magneto-optical spectroscopy of Co_2FeSi Heusler compound, J. Appl. Phys. **115**, 17A927 (2014).

[36] B. Sepúlveda, Y. Huttel, C. Martínez Boubeta, A. Cebollada, and G. Armelles, Linear and quadratic magnetooptical Kerr effects in continuous and granular ultrathin monocrystallineFe films, Phys. Rev. B **68**, 064401 (2003).

[37] I. D. Lobov, A. A. Makhnev, and M. M. Kirillova, Optical and magnetooptical properties of Heusler alloys XMnSb (X = Co, Pt), Phys. Met. Metalloved. **113**, 135 (2012).

[38] M. Buchmeier, R. Schreiber, D. E. Bürgler, and C. M. Schneider, Thickness dependence of linear and quadratic magneto-optical Kerr effects in ultrathin Fe(001) films, Phys. Rev. B **79**, 064402 (2009).

[39] T. Kuschel, H. Bardenhagen, H. Wilkens, R. Schubert, J. Hamrle, J. Pištora, and J. Wollschläger, Vectorial magnetometry using magnetooptic Kerr effect including first- and second-order contributions for thin ferromagnetic films, J. Phys. D: Appl. Phys. **44**, 265003 (2011).

[40] J. Hamrlová, J. Hamrle, K. Postava, and J. Pištora, Quadratic-in-magnetization permittivity and conductivity tensor in cubic crystals, Phys. Status Solidi B **250**, 2194 (2013).

[41] N. Nagaosa, J. Sinova, S. Onoda, A. H. MacDonald, and N. P. Ong, Anomalous Hall effect, Rev. Mod. Phys. **82**, 1539.

[42] W. Thomson, On the electro-dynamic qualities of metals: Effects of magnetization on the electric conductivity of nickel and of iron, Proc. R. Soc. London **8**, 546 (1857).

[43] P. Kühne, C. M. Herzinger, M. Schubert, J. A. Woollam, and T. Hofmann, Invited article: An integrated mid-infrared, far-infrared, and terahertz optical hall effect instrument, Rev. Sci. Instrum. **85**, 071301 (2014).

[44] J. Chochol, K. Postava, M. Čada, M. Vanwolleghem, L. Halagačka, J.-F. Lampin, and J. Pištora, Magneto-optical properties of InSb for terahertz applications, AIP Adv. **6**, 115021 (2016).

[45] S. Valencia, A. Kleibert, A. Gaupp, J. Rusz, D. Legut, J. Bansmann, W. Gudat, and P. M. Oppeneer, Quadratic X-Ray Magneto-Optical Effect Upon Reflection in a Near-Normal-Incidence Configuration at the M edges of 3D-Transition Metals, Phys. Rev. Lett. **104**, 187401 (2010).

[46] H.-Ch. Mertins, P. M. Oppeneer, J. Kuneš, A. Gaupp, D. Abramsohn, and F. Schäfers, Observation of the X-Ray Magneto-Optical Voigt Effect, Phys. Rev. Lett. **87**, 047401 (2001).

[47] A. von Ettingshausen and W. Nernst, Ueber das Auftreten electromotorischer Kräfte in Metallplatten, welche von einem Wärmestrome durchflossen werden und sich im magnetischen Felde befinden, Ann. Phys. Chem. **265**, 343 (1886).

[48] S. Y. Huang, W. G. Wang, S. F. Lee, J. Kwo, and C. L. Chien, Intrinsic Spin-Dependent Thermal Transport, Phys. Rev. Lett. **107**, 216604 (2011).

[49] D. Meier, T. Kuschel, L. Shen, A. Gupta, T. Kikkawa, K. Uchida, E. Saitoh, J.-M. Schmalhorst, and G. Reiss, Thermally driven spin and charge currents in thin $NiFe_2O_4$/Pt films, Phys. Rev. B **87**, 054421 (2013).

[50] M. Schmid, S. Srichandan, D. Meier, T. Kuschel, J.-M. Schmalhorst, M. Vogel, G. Reiss, C. Strunk, and C. H. Back, Transverse Spin Seebeck Effect versus Anomalous and Planar Nernst Effects in Permalloy Thin Films, Phys. Rev. Lett. **111**, 187201 (2013).

[51] D. Meier, D. Reinhardt, M. Schmid, C. H. Back, J.-M. Schmalhorst, T. Kuschel, and G. Reiss, Influence of heat flow directions on Nernst effects in Py/Pt bilayers, Phys. Rev. B **88**, 184425 (2013).

[52] O. Reimer, D. Meier, M. Bovender, L. Helmich, J.-O. Dreessen, J. Krieft, A. S. Shestakov, C. H. Back, J.-M. Schmalhorst, A. Hütten, G. Reiss, and T. Kuschel, Quantitative separation of the anisotropic magnetothermopower and planar Nernst effect by the rotation of an in-plane thermal gradient, Sci. Rep. **7**, 40586 (2017).

[53] Š. Višňovský, *Optics in Magnetic Multilayers and Nanostructures* (CRC Press, Boca Raton, 2006).

[54] E. Hecht, *Optics*, 4th ed. (Addison Wesley, San Francisco, 2002).

[55] R. Silber, Quadratic-in-magnetization magneto-optical spectroscopy, Master's thesis, VŠB - Technical University of Ostrava, 2014.

[56] M. Björck and G. Andersson, GenX: an extensible X-ray reflectivity refinement program utilizing differential evolution, J. Appl. Crystallogr. **40**, 1174 (2007).

[57] L. G. Parratt, Surface Studies of Solids by Total Reflection of X-Rays, Phys. Rev. **95**, 359 (1954).

[58] W. M. Haynes, D. R. Lide, and T. J. Bruno, *Handbook of Chemistry and Physics*, 95th ed. (CRC press, Boca Raton, 2014).

[59] J. S. Custer, M. O. Thompson, D. C. Jacobson, J. M. Poate, S. Roorda, W. C. Sinke, and F. Spaepen, Density of amorphous Si, Appl. Phys. Lett. **64**, 437 (1994).

[60] G. Mende, J. Finster, D. Flamm, and D. Schulze, Oxidation of etched silicon in air at room temperature; Measurements with ultrasoft X-ray photoelectron spectroscopy (ESCA) and neutron activation analysis, Surf. Sci. **128**, 169 (1983).

[61] P. Yeh, Optics of anisotropic layered media: A new 4×4 matrix algebra, Surf. Sci. **96**, 41 (1980).

[62] J. A Woollam Co., Inc., *CompleteEASE*^{TM} *Data Analysis Manual* (2008).

[63] E. D. Palik, *Handbook of Optical Constants of Solids* (Academic Press, San Diego, 1985).

[64] B. Johs and J. S. Hale, Dielectric function representation by B-splines, Phys. Status Solidi A **205**, 715 (2008).

[65] R. Silber, M. Tomíčková, J. Rodewald, J. Wollschläger, J. Pištora, M. Veis, T. Kuschel, and J. Hamrle, Quadratic magnetooptic spectroscopy setup based on photoelastic light modulation, Phot. Nano. Fund. Appl. **31**, 60 (2018).

[66] H. T. Yolken and J. Kruger, Optical Constants of Iron in the Visible Region, J. Opt. Soc. Am. **55**, 842 (1965).

[67] P. B. Johnson and R. W. Christy, Optical constants of transition metals: Ti, V, Cr, Mn, Fe, Co, Ni, and Pd, Phys. Rev. B **9**, 5056 (1973).

[68] J. H. Liang, X. Xiao, J. X. Li, B. C. Zhu, J. Zhu, H. Bao, L. Zhou, and Y. Z. Wu, Quantitative study of the quadratic magneto-optical Kerr effects in Fe films, Opt. Express **23**, 11357 (2015).

[69] O. Stejskal, R. Silber, J. Pištora, and J. Hamrle, Convergence study of the *ab initio* calculated quadratic magneto-optical spectra in bcc Fe, Phot. Nano. Fund. Appl. **32**, 24 (2018).

[70] P. Blaha, K. Schwarz, G. Madsen, D. Kvasnicka, and J. Luitz, *User's Guide, WIEN2k_16.1 (Release 10/15/2014)*, Vienna University of Technology, Austria (2014).

[71] C. Ambrosch-Draxl and J. O. Sofo, Linear optical properties of solids within the full-potential linearized augmented planewave method, Comput. Phys. Commun. **175**, 1 (2006).

[72] J. Hamrlová, D. Legut, M. Veis, J. Pištora, and J. Hamrle, Principal spectra describing magnetooptic permittivity tensor in cubic crystals, J. Magn. Magn. Mater. **420**, 143 (2016).

[73] O. Miura and T. Fujiwara, Electronic structure and effects of dynamical electron correlation in ferromagnetic bcc Fe, fcc Ni, and antiferromagnetic NiO, Phys. Rev. B **77**, 195124 (2008).

[74] Y. Yao, L. Kleinman, A. H. MacDonald, J. Sinova, T. Jungwirth, D.-S. Wang, E. Wang, and Q. Niu, First Principles Calculation of Anomalous Hall Conductivity in Ferromagnetic bcc Fe, Phys. Rev. Lett. **92**, 037204 (2004).

[75] See Supplemental Material at http://link.aps.org/supplemental/10.1103/PhysRevB.100.064403 for data files of ε_d, K, G_s, and $2G_{44}$ spectra.

[76] P. Granberg, P. Isberg, T. Baier, B. Hjörvarsson, and P. Nordblad, Anisotropic behavior of the magnetoresistance in single crystalline iron films, J. Magn. Magn. Mater. **195**, 1 (1999).